Lithos 314–315 (2018) 360–381

Contents lists available at ScienceDirect

Lithos

journal homepage: www.elsevier.com/locate/lithos

# REE mineralisation within the Ditrău Alkaline Complex, Romania: Interplay of magmatic and hydrothermal processes

V.C. Honour [a,b,*], K.M. Goodenough [c], R.A. Shaw [d], I. Gabudianu [e], P. Hirtopanu [f]

[a] Department of Earth Sciences, University of Cambridge, Cambridge CB2 3EQ, UK
[b] Camborne School of Mines, University of Exeter, Penryn, Cornwall TR10 9FE, UK
[c] British Geological Survey, The Lyell Centre, Research Avenue South, Edinburgh EH14 4AP, UK
[d] British Geological Survey, Environmental Science Centre, Keyworth, Nottingham NG12 5GG, UK
[e] 11th Prahova Street, 012424 Bucharest, Romania
[f] Department of Mineralogy, University of Bucharest, Romania

ARTICLE INFO

*Article history:*
Received 12 November 2017
Accepted 29 May 2018
Available online xxxx

*Keywords:*
Ditrău Complex, Romania
Alkaline intrusion
Late-stage magmatic fluids
REE mineralisation

ABSTRACT

The Ditrău Igneous Complex (north-east Romania) is a tilted Mesozoic alkaline intrusion (~19 km diameter), with enrichments in rare earth elements (REE), niobium, and molybdenum. It has the potential to contribute to a secure and sustainable European REE mining industry, ensuring supply security for these critical metals. The complex comprises a sequence of ultramafic rocks, alkali gabbros, diorites, syenites, nepheline syenites and alkali granites. These units have been significantly modified by sub-solidus interaction with late-stage magmatic fluids and are cut by secondary mafic dykes. The complex was subsequently cut by REE-mineralised carbonate-rich veins. Geochemical and petrological data, including apatite mineral chemistry, from the alkaline igneous rocks, dykes and veins within the Ditrău Complex, have been used to assess the interplay of magmatic processes with late-stage magmatic and hydrothermal fluids, and the effects of these processes on element remobilisation and concentration of critical metals. Only limited critical metal enrichment was achieved by magmatic processes; the REE were preferentially incorporated into titanite and apatite in ultramafic cumulates during primary crystallisation, and were not enriched in evolved magmas. A hydrothermal system developed within the Ditrău Complex magma chamber during the later stages of magmatic crystallisation, causing localised alteration of nepheline syenites by a sodium-rich fluid. Mafic dykes subsequently acted as conduits for late stage, buoyant potassic fluids, which leached REE and HFSE from the surrounding syenitic rocks. These fluids percolated up and accumulated in the roof zone, causing the breakdown of nepheline to K-rich pseudomorphs and the precipitation of hydrothermal minerals such as zircon and pyrochlore within veins. REE mineralisation within the Ditrău Complex is hosted in the latest hydrothermal phase, mineralised carbonate-rich veins, which cross-cut the complex. Monazite is the main REE-bearing phase, it crystallised from a late REE- and carbonate-rich fluid with pH controlled REE deposition.



## 1. Introduction

Rare earth elements (REE) and other 'critical metals' are vital to many of today's technologies, crucial to providing competitive, yet sustainable economic growth. Within the European Union, REE have significant economic importance, but clear supply risks, pushing them onto the critical metals agenda and ensuring a focus from the European Commision (2017). Recycling of REE is minimal, and substitutes are generally less effective (Binnemans et al., 2013), so future supply will require primary extraction (U.S. Geological Survey, 2015). In 2017, China supplied 95% of the world's REE (European Commision, 2017). Europe's rare earth resources are under-studied with no current production from primary resources; however, domestic deposits have the potential to supply Europe's REE demands for the foreseeable future (Goodenough et al., 2016). The European Commission-funded EURARE project (www.eurare.org) aimed to establish the basis for sustainable REE mining and production within Europe, thus increasing supply security.

The most studied REE deposits in Europe are associated with carbonatites (e.g. Fen in Norway) or highly peralkaline igneous rocks e.g. Norra Kärr in Sweden, Kvanefjeld and Kringlerne in the Ilímaussaq Complex of Greenland (Goodenough et al., 2016). REE mineralisation can also occur in hydrothermally altered alkaline igneous rocks (Chakhmouradian and Wall, 2012). In this paper we describe one such intrusion with late-stage hydrothermal REE mineralisation: the Ditrău Complex in eastern Transylvania, Romania (Fig. 1).

* Corresponding author at: Department of Earth Sciences, University of Cambridge, Cambridge CB2 3EQ, UK.
*E-mail address:* vch28@cam.ac.uk (V.C. Honour).

https://doi.org/10.1016/j.lithos.2018.05.029

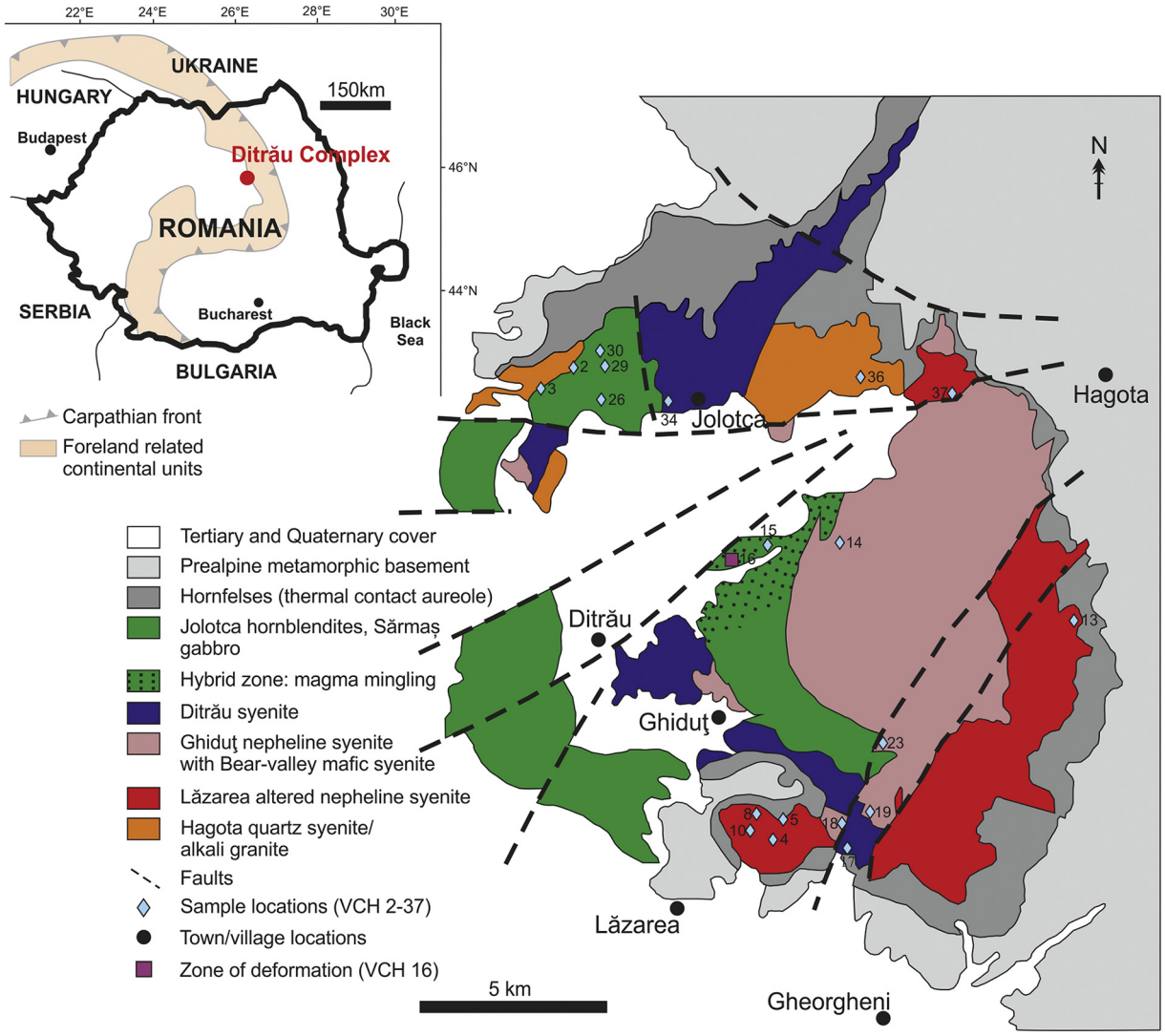


**Fig. 1.** Adapted geological map after Kräutner and Bindea (1998), based on fieldwork observations and lithology nomenclature from this study. Inset shows the position of the Ditrău Complex in Romania.

The Ditrău Complex is a Triassic alkaline intrusion (Pană et al., 2000) with REE, niobium and molybdenum mineralisation (Hirtopanu et al., 2010). The complex is cut by multiple dykes (Batki et al., 2014) and carbonate veins, 1–2 m wide, which host REE mineralisation. This paper characterises the origin of the REE mineralisation and its association with hydrothermal fluids within the Ditrău Complex. New geochemical and petrological data for key lithologies and mineralised material are correlated with field relationships to provide an integrated overview of the REE mineralisation, in the context of the magmatic and hydrothermal system.

## 2. Geological background

The Ditrău Complex intruded in the mid-Triassic, during extensional activity associated with Tethyan rifting (Pál-Molnár and Avra-Sós, 1995; Pană et al., 2000). Unlike the voluminous Central Atlantic Magmatic Province, the Alpine Tethyan rifting generated minimal magmatic activity (Stampfli, 2000), so the Ditrău Complex is not part of a recognised alkaline province. The complex is exposed over an area 19 by 14 km and intrudes Variscan-metamorphosed Precambrian and Cambrian crystalline basement rocks of the Bucovinian nappe within the Eastern Carpathians; further details on the structural setting are provided by Pál-Molnár et al. (2015a).

From the mid-Cretaceous to Tertiary the region was deformed by Alpine tectonic events, forming a nappe system (Dewey et al., 1973). Today the complex is partially obscured by Cenozoic magmatism (Szakacs et al., 1997) and Pliocene-Pleistocene sediments and lacustrine deposits (Codarcea et al., 1957).

The complex has previously been hypothesised as a ring structure (Zincenco and Vlad, 1978) with successively younger intrusions becoming more felsic from west to east: ultramafics, alkali gabbros and diorites out crop in the north-west whereas syenites, nepheline syenites and alkali granites lie to the south-east (Morogan et al., 2000; Pál-Molnár et al., 2015a). Lamprophyre dykes represent a basanitic melt that has penetrated the complex (Batki et al., 2014; Pál-Molnár et al., 2015a).

Key geographical areas of the Ditrău Complex are: the northern area around the village of Jolotca (the Jolotca region); the main area, lying to the east of the village of Ditrău (the Ditrău region); and the southern region of Lăzarea. Jolotca and Ditrău are separated by a zone of faulting (Fig. 1).

The Jolotca area is characterised by outcrops of mafic–ultramafic cumulate igneous rocks, including alkali gabbro and alkali diorite (Morogan et al., 2000; Pál-Molnár, 2000; Pál-Molnár et al., 2015a). These rocks are inferred, on the basis of gravity and magnetic surveys, to extend laterally eastward beneath the complex (Jakab, 1998). In the centre of the complex there is a hybrid zone of magma mingling and

igneous brecciation that includes gabbroic, dioritic and syenitic lithologies; this combination is referred to by Streckeisen (1960) as the 'Ditró essexites' (Table 1).

The east of the complex is dominated by felsic rocks (syenites, nepheline syenites and alkali granites) which show varying degrees of alteration (Jakab, 1998; Morogan et al., 2000). Previously the undersaturated syenites of the complex have been divided into 'White Syenite' and 'Red Syenite' (Jakab, 1998). The 'Red Syenite' forms patchy bodies within the 'White Syenite'. Morogan et al. (2000) and Fall et al. (2007) refer to the 'White Syenite' as nepheline syenite. The 'Red Syenite' is enriched in HFSE-bearing minerals and Jakab (1998) describes micaceous aggregates pseudomorphing nepheline. He suggested that 'Red Syenite' is hydrothermally altered to 'White Syenite' based on relict structures and the lower volume of 'Red Syenite' observed in drill-core; however, Morogan et al. (2000) consider the nepheline syenite to have been hydrothermally altered to 'Red syenite'. In this paper, a revised terminology is proposed, as described below.

Numerous genetic models have been suggested for the Ditrău Complex. These include metasomatism by a Na-rich fluid permeating the country rock (Codarcea et al., 1957); magmatic differentiation of an alkali parent magma (Streckeisen, 1960); partial-melting of silica-poor crustal rocks producing a basic magma and a sialic alkaline magma (Anastasiu and Constantinescu, 1982); and a two stage emplacement process (Pál-Molnár and Avra-Sós, 1995). This last model was superseded by a four stage model, which compiled all isotope dates on the complex to suggest that emplacement of the Ditrău intrusion spanned a 70 Myr interval across the Triassic and Jurassic (Kräutner and Bindea, 1998). The stages described are: (1) c. 230 Ma: mafic and ultramafic intrusions in the Jolotca region, dated by four K-Ar analyses and two hornblende $^{40}Ar$-$^{39}Ar$ ages of 231.5 and 227.1 ± 0.1 Ma (Dallmeyer et al., 1997). (2) c. 215 Ma: gabbros, diorites, monzodiorites, monzonites, syenites and quartz syenites (Kräutner and Bindea, 1998). (3) c. 165–160 Ma: intrusion of nepheline syenites and formation of 'Ditró essexites' (Streckeisen, 1960), followed by a series of dyke intrusions. These lithologies were dated by K-Ar on biotite in nepheline syenite (Streckeisen and Hunziker, 1974). (4) c. 115 Ma: final hydrothermal activity associated with nappe transport due to tectonic uplift. More recently, Batki et al. (2018) suggested two major magma sources contributed to magmatic processes at Ditrău.

These past models were based on isotope ages from the $^{40}Ar/^{39}Ar$, K-Ar and Rb/Sr systems, with the ages given direct geochronological legitimacy despite the limited precision of some of the analyses (Dallmeyer et al., 1997; Pál-Molnár and Avra-Sós, 1995; Streckeisen and Hunziker, 1974). The inconsistencies, spread of data and potential for disrupted Ar degassing due to Alpine tectonics, make the models based on these ages "highly suspect" (Pană et al., 2000). Pană et al. (2000) used U-Pb zircon ages to date a sample of syenite from near the Jolotca village at 229.6 + 1.7/−1.2 Ma. The $^{40}Ar$-$^{39}Ar$ dates produced by Dallmeyer et al. (1997) are within error of these U-Pb zircon ages, indicating contemporaneous emplacement of syenite and gabbroic magmas, with a relatively short magmatic evolution of the Ditrău Complex.

The igneous rocks of the Jolotca area are cut by veins hosting REE mineralisation, generally up to 1 m wide, trending E-W and dipping 60°N (Jakab and Cernaianu, 2015, pers. comm.). The mineralogy comprises LREE-phosphates, LREE-silicates and LREE-carbonates, with pyrite, molybdenite, Ta- and Nb-bearing phases, all hosted in a carbonate gangue (Hirtopanu et al., 2010; Săbău, 2009). In the south-east, 2.5 km outside the Ditrău Complex lies another area of vein-hosted mineralisation, named Belcina. Mineralisation at Belcina is analogous to the mineralised veins at Jolotca. The Belcina veins comprise Y-phosphates, Th-silicates, zircon, minor sulfides, and Ta- and Nb-bearing phases in a carbonate gangue (Hirtopanu et al., 2013b).

These mineralised veins were investigated during government-led exploration in the 20th century. Five deep (c. 1400 m) cores were drilled and there are multiple historic adits (with associated waste dumps) in the Jolotca region, but none are accessible. The majority of drill-core has been lost or remains under state ownership with restricted access. There is a limited selection at the geological museum in Gheorgheni, Romania.

**Table 1**
A summary of previously published lithology names, compared to the new lithodemic classification provided by this paper.

| Unit name in literature | This paper | Reference |
|---|---|---|
| Amphibole- and pyroxene-rich cumulate | Jolotca hornblendite | Pál-Molnár et al., 2015a; Pál-Molnár, 2000 |
| Alkali gabbro I/Amphibole- and pyroxene-rich cumulate | Sărmaş gabbros | Morogan et al., 2000; Fall et al., 2007; Pál-Molnár et al., 2015a; Batki et al., 2018 |
| Alkali diorite | Bear-valley mafic syenite | Morogan et al., 2000 |
| Ditró essexites/mixed diorite-gabbro-syenite zone/Alkali gabbro II | Hybrid zone | Streckeisen, 1960/ Morogan et al., 2000 |
| Syenite-monzosyenite | Ditrău syenite | Kräutner and Bindea, 1998; Morogan et al., 2000 |
| White syenite/Detroite/Nepheline syenite | Ghiduţ nepheline syenite | Jakab, 1998/ Morogan et al., 2000; Fall et al., 2007 |
| Red syenite/"red, hydrothermally altered variety" of nepheline syenite | Lăzarea altered nepheline syenite (LANS) | Jakab, 1998/ Morogan et al., 2000 |
| Quartz syenites | Hagota quartz syenite | Jakab, 1998; Morogan et al., 2000; Pál-Molnár, 2000 |
| Mafic dykes/Camptonite dykes | Mafic dykes | Morogan et al., 2000/ Batki et al., 2014 |
| Mineralised veins hosted in a carbonate gangue | Mineralised veins | Săbău, 2009; Hirtopanu et al., 2010; Hirtopanu et al., 2013a |

## 3. Geology of the complex

Previous work has focused on the age and petrogenesis of the igneous rocks, or the mineralogy of the REE veins, but the hydrothermal alteration and relationship between the two have not been fully described. This section lays out our understanding of the Ditrău Complex, drawing together magmatic and hydrothermal processes, based on published literature and fieldwork during summer 2015. The Ditrău Complex is characterised by moderate topography, with grass-covered hills and woodland. Outcrops are largely found in valleys, road cuts, old quarries, and mine dumps adjacent to adits.

The complex is exposed such that outcrops provide a transect from ultramafic-mafic cumulate rocks to nepheline syenites and quartz syenites. Previous publications have used a wide variety of unit names (Fall et al., 2007; Jakab, 1998; Morogan et al., 2000; Pál-Molnár et al., 2015a). Consequently, it has been necessary to propose a new set of lithological units that encompass both magmatic and hydrothermal processes (Table 1); the formal lithodemic classification for this work is based on non-genetic, descriptive field observations, supplemented by optical microscopy and previous literature. These units are described below and their distribution is shown on Fig. 1.

### 3.1. Jolotca hornblendite

The Jolotca hornblendite is a black, medium-grained, amphibole-dominated, locally foliated ultramafic rock, found as discrete bodies in association with the gabbros and syenodiorites of the Jolotca region. These essentially mono-mineralic rocks are described in detail by Pál-Molnár et al. (2015a). Accessory minerals include randomly oriented cumulus titanite, up to 1 cm long (Fig. 2(a)). In-situ exposures are typically highly weathered; however, the mine waste dumps have fresh

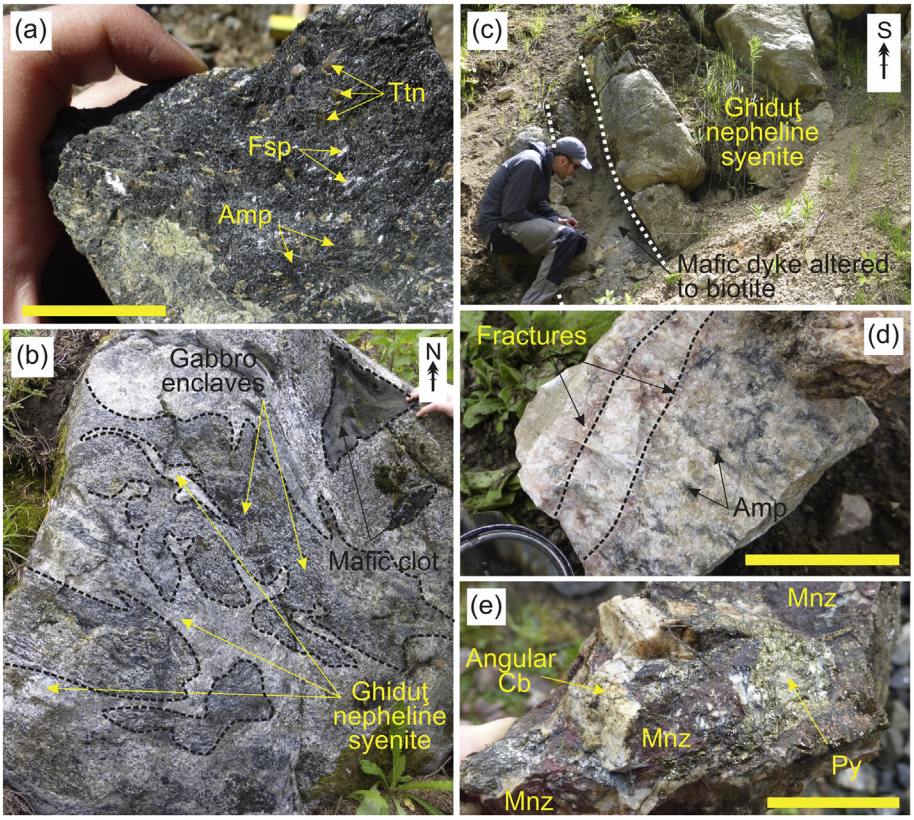


**Fig. 2.** Field photos from the Ditrău Complex. (a) Jolotca hornblendite containing large titanites. (b) Magma mingling in the Ditrău valley between Ghiduț nepheline syenite and Sărmaș gabbro. (c) Altered mafic dyke cutting the Ghiduț nepheline syenite in the Ditrău valley. (d) Lăzarea altered nepheline syenite with fractures defined by red minerals, from the Lăzarea region. (e) Mineralised vein hosting monazite and pyrite in a carbonate gangue, from a waste dump in Jolotca. Mineral abbreviations from Whitney and Evans (2010). (For interpretation of the references to colour in this figure legend, the reader is referred to the web version of this article.)

examples. Carbonate veins (<2 mm wide) are common, as are pegmatitic and aplitic syenite veins (5–20 cm wide).

### 3.2. Sărmaș gabbro

Gabbros are exposed in the Jolotca region, around Ditrău and in the limited drill-core held in the Gheorgheni museum, Romania. The freshest samples are blocks (10–80 cm) from mine waste dumps.

The gabbros vary from medium- to coarse-grained within the Jolotca and Ditrău region, and are characterised by varying proportions of granular amphibole, plagioclase and titanite, with accessory magnetite, apatite and zircon. The gabbros have a variably present, weak foliation. This unit is described by Pál-Molnár et al. (2015a) as an amphibole- and pyroxene-rich cumulate and is comparable to the alkali gabbro I of Morogan et al. (2000) and the alkali gabbros from drill-cores (Jakab, 1998).

#### 3.2.1. Gabbro hybrid units

In the hybrid zone east of Ditrău, gabbros are net-veined by coarse-grained nepheline syenite, forming rounded to sub-angular gabbroic enclaves, with sharp boundaries but no chilled or baked margins (Fig. 2(b)). Occasional gabbro-syenite contacts are diffuse over a few centimetres, with partially disaggregated enclaves. Locally within the enclaves are hornblendite clots up to 10 cm wide. This zone shows significant variations in deformation state; the magmatic textures grade, over hundreds of metres, into intensely foliated and deformed lithologies that are well-exposed in roadside outcrops (locality VCH-16; Supplementary Table 1).

Streckeisen (1960) referred to the hybrid outcrops as 'Ditró essexites' (Table 1). The evidence is consistent with magma mingling, and does not support Jakab (1998) proposal that the 'essexites' were formed by metasomatism of country rock.

### 3.3. Ditrău syenite

The Ditrău syenite lies chiefly on the western side of the complex with good exposure in the Jolotca and Lăzarea areas. It is a mela-syenite, ranging from medium (1–5 mm) to coarse-grained (>5 mm) and is dominated by tabular alkali feldspars, amphiboles (<1 cm wide), biotite, accessory titanite (<5 mm) and magnetite. The Ditrău syenite is heterogeneous, locally becoming more dioritic with increasing amounts of modal amphibole (15–40%). Nepheline and HFSE-rich accessory minerals are notably absent. The syenitic texture varies from massive to foliated, with an igneous foliation defined by euhedral feldspars and amphibole. The lithology is cut by abundant aplitic veins (1–3 cm wide) and fine-grained mafic dykes. The Ditrău syenite as defined here, encompasses the rock-types described as syenite-monzosyenite by Kräutner and Bindea (1998) and Morogan et al. (2000).

### 3.4. Ghiduț nepheline syenite

Nepheline syenites are dominant in the central and eastern areas of the Ditrău Complex, near to the village of Ghiduț. The nepheline syenite is white and generally massive (Fig. 2(c)). The modal mineralogy is spatially heterogeneous on the scale of tens of metres, and can grade into a more mafic syenite.

The Ghiduț nepheline syenite is granular and characterised by medium- to very coarse-grained tabular alkali feldspar (<4 cm) and large (1–2 cm) euhedral nepheline. Nepheline is locally altered to cancrinite, and yellow rims around nepheline grains are visible in hand specimen. Sodalite typically follows 2–3 mm wide fractures, and is also found

around feldspars and nepheline. Amphibole and biotite are present (<20%) in medium-grained nepheline syenites, but not in the coarsest varieties. The Ghiduţ nepheline syenite is equivalent to the 'Ditroite' and the white nepheline syenites (Table 1), described by Jakab (1998), Morogan et al. (2000) and Fall et al. (2007).

A 40 m wide exposure was observed in a quarry within the Ditrău Valley (locality VCH-14; Supplementary Table 1). The outcrop has a set of steeply westward dipping fractures. A weathered biotite-rich dyke (0.3 m wide) cuts the Ghiduţ nepheline syenite parallel with the fractures (Fig. 2(c)). There is a 20 m transition zone in the quarry, from fresh nepheline syenite to an altered variant surrounding the dyke. The Ghiduţ nepheline syenite in close proximity (<2 m) to the dyke contains large biotites and zircons (<1 cm) and greenish mica aggregates replacing nephelines. The mafic dyke is highly altered to biotite, and similar features are seen elsewhere in the complex.

#### 3.4.1. Bear-valley mafic syenite

The Bear-valley mafic syenite is an end member of the Ghiduţ nepheline syenite, but exposure is limited. Samples were collected in the centre of the complex and towards the Lăzarea region. The mafic syenite contains minimal nepheline, and has >35% mafic minerals. The mafic syenite is medium- to coarse-grained with a foliation defined by mafic minerals. Amphibole-rich clots (2–4 cm in width) are found within the Bear-valley mafic syenite.

### 3.5. Lăzarea altered nepheline syenite (LANS)

The LANS predominates along the south-easterly margin of the Ditrău Complex. It was previously named the 'Red syenite' (Jakab, 2015, pers. comm.) and the "red, hydrothermally altered variety" of nepheline syenite (Morogan et al., 2000). Haematite gives the characteristic red colour, but this colouration is not always indicative of, nor essential to, the LANS. Variation in alteration of the LANS is seen in mine dumps in the east of the intrusion (locality VCH-13; Supplementary Table 1; Fig. 2(d)). In-situ exposures of LANS are rare, but there are small outcrops on hills north-east of Lăzarea and along road cuts in the north-east of the complex.

Grain size is variable, fluctuating from coarse- to very coarse-grained (5 to >10 mm respectively). The LANS is characterised by dull green micaceous pseudomorphs after nepheline (0.2–3 cm), large alkali feldspars (0.5–1 cm) and up to 15% mafic minerals (biotite and amphibole). The proportion of mafic minerals decreases to 5% as grain size increases. Molybdenite is generally found along fractures, and in association with fluorite in the east of the complex.

Locally the LANS has a foliation defined by mafic phases; it is strongest in the medium-grained syenite. The unit is cut by a variety of veins and fractures, often with haematised margins (Fig. 2(f)). Felsic veins (aplitic and pegmatitic), mafic veins (microdiorite, hornblendite and biotite), sulfide-rich veins and carbonate veins, 0.3–10 cm wide, cut the foliation. The felsic veins often have an abundance of accessory minerals (e.g. zircon, pyrochlore, and apatite).

### 3.6. Hagota quartz syenite

Quartz syenites are found in the Jolotca area and north-east of the complex (Jakab, 1998; Morogan et al., 2000; Pál-Molnár, 2000). They are massive, medium-grained rocks of alkali feldspar and quartz with accessory biotite. Granites have also been described (Morogan et al., 2000; Pál-Molnár et al., 2015b), but are not discussed here.

### 3.7. Mafic dykes

Fine-grained mafic dykes (15–50 cm wide) cut the major lithologies. Studies by Batki et al. (2014) and Anastasiu and Constantinescu (1982) report extensively on the lamprophyres occurring in the northern part of the complex. The mafic dykes sampled in this study were from the Ditrău valley (in the centre of the complex) and were typically altered, but most likely of lamprophyre origin. They are dark grey and characterised by fine-grained feldspar (<5%) and amphibole, with amphibole replaced by biotite at altered margins (Fig. 2(c)). This forms a 'friable' texture, which variably extends to the dyke centre.

### 3.8. Mineralised veins

Mineralised veins with a carbonate gangue cut the mafic-ultramafic lithologies in the Jolotca region, and the country rock in the Belcina region. No in-situ outcrops have been found within the Jolotca region and therefore the characteristics described are from mine dump samples. Jakab (2015, pers. comm.) described the carbonate mineralised veins at Jolotca as typically 1 m wide, trending E-W, parallel with the Jolotca valley and dipping 60°N. Previous mineral exploration suggests that faulting has offset the veins (Jakab, 2015, pers. comm.).

A range of minerals have been described from the veins (Hirtopanu et al., 2010, 2013a, 2015; Jakab, 1998); rutile, monazite (Fig. 2(e)) and pyrite are recognisable in hand specimen in the Jolotca area. The veins in the Belcina area are highly radioactive so samples could not be safely obtained.

### 3.9. Structure of the complex

Previous authors have suggested that the Ditrău Complex represents a ring intrusion (e.g. Morogan et al., 2000; Zincenco and Vlad, 1978), although the presence of cumulate structures has been recognised (e.g. Morogan et al., 2000; Pál-Molnár et al., 2015a). We consider the field evidence to be more consistent with emplacement in a broadly horizontal magma chamber that has subsequently been tilted towards the east. Although the Carpathian Cenozoic thrust systems are east-facing, the Bucovinian nappe has been folded during Cenozoic thrusting (Matenco et al., 2010), and the tilting of the Ditrău Complex may well be attributable to this folding. The mafic-ultramafic cumulates (the Jolotca hornblendite and Sărmaş gabbro) show clear banding and foliation dipping broadly eastward, and are considered here to represent the original lower part of the magma chamber. The evidence of extensive hybridisation in the central part of the magma chamber (gabbro hybrids) indicates more highly evolved magmas mixing and mingling with the mafic crystal mush. The Ghiduţ nepheline syenite represents the most highly evolved magmas in the upper part of the chamber. The LANS represents an intensely altered roof zone.

A zone of deformation transects the complex, running north-east from the town of Ditrău. Much of this zone is covered by younger sediments, but where outcrops are exposed the gabbros and gabbro hybrids are seen to be strongly deformed, near-mylonitic. Relatively undeformed syenitic veins cut across this deformation fabric, indicating that the fabric formed within the magma chamber. The high-temperature deformation within these outcrops most likely indicates a zone of active shearing within the mush, which has been subsequently reactivated by later faulting. Brittle faults and fractures are common within the complex.

## 4. Samples and analytical methods

We collected forty-six samples from thirty-eight localities in the complex, representing key lithologies (Supplementary Table 1). Fieldwork focused on two areas: (1) the Jolotca region in the north-west, and (2) the southern area. The samples covered a range of lithologies and alteration products. Samples were characterised at the British Geological Survey (BGS), Keyworth using a Zeiss Axioplan 2 imaging microscope and two SEMs for semi-quantitative mineral compositions, element EDS X-ray maps and back-scatter electron (BSE) imagery: (1) an FEI Company Quanta 600 environmental scanning electron microscope (ESEM) equipped with an Oxford Instruments INCA Energy 450 energy-dispersive X-ray microanalysis system (EDXA), set to 20 kV at

1.2 nA, with a working distance of 10 mm; and (2) a LEO 435VP variable pressure digital SEM, using Oxford Instruments INCA EDXA system, set to 20 kV at 0.5 nA and a working distance of 19 mm.

Twenty rock powder samples were prepared using a chrome steel jaw crusher and ground using an agate milling vessel. Major element whole rock analyses were obtained by fused bead XRF by PANalytical at the BGS, Keyworth. The analyses were conducted using a PANalytical Axios sequential fully automatic wavelength-dispersive X-ray fluorescence spectrometer. Loss on ignition ranges from 0.4–3.6% with final totals within the range, 99–101%.

Whole rock analyses for a suite of fifty-four minor and trace elements were obtained by Inductively Coupled Plasma Mass Spectrometry (ICP-MS) using dissolution by Na-peroxide fusion to ensure resistant accessory minerals were fully digested. ICP-MS analyses were carried out at the BGS, Keyworth, on an Agilent 7500cx series machine, calibrated using known concentrations in solution of the analysed elements. The results had good precision: elements of interest (Hf, U, Th, Mo, Sr, Y, Zr, Nb, REE, and Ta) have a relative percentage difference typically below 10% between duplicate sample pairs. Sm, Eu, Ho and Mo have a slightly higher relative percentage difference between 10% and 20%. Four certified reference materials of varying composition (syenite powder, GSR-7; andesite, AGV-2; Columbia River basalt, BCR-2; and diorite gneiss, SY-4) were analysed. All trace elements of interest were within 10% of certified reference values, except for U, Th, Ta, Gd and Zr, which were within 15%.

Apatite compositions were measured using a Cameca SX100 electron microprobe equipped with five wavelength-dispersive spectrometers at the Grant Institute of Earth Science, University of Edinburgh. Two analytical condition routines were run: a light element analysis followed by a heavy element analysis. The instrument uses Cameca's PeakSight software, with ZAF correction. The light element analytical routine was run at 20 kV, 10 nA with a 12 μm defocused spot to analyse: F, Cl, Na, P and Ca. Na was measured for 60 s on peak, the rest for 20 s. These conditions minimise the potential for halogen migration during apatite analysis by EPMA (Stock et al., 2015; Stormer et al., 1993). The heavy element routine was run at 20 kV, 80 nA with a 12 μm spot to analyse: Al, Si, S, Mn, Sr, La, Y, Ce, Fe, Pr, Nd and Y. Mn was measured for 90 s on peak, Sr for 20 s, Ce for 30 s, Y for 120 s and the rest for 60 s. Oriented apatite secondary standards (Durango and Wilberforce) were regularly run and had good precision. The two standard deviations relative percentage for the unknowns is below 5% for F, P, Ca, Si and Ce; below 10% for Mn, Sr, La, Y, Fe and Nd. It is 42% for Pr. Na, Cl, S and Pr reach concentrations 3.3 times detection limit in selected lithologies. Over 280 apatite analyses were performed, mostly from apatite cores, on eight different samples. The apatite analysis totals have been recalculated accounting for mixing on the monovalent anion sites (e.g. $F^-$, $Cl^-$ and $OH^-$). Some apatite analyses had low totals; this is likely due to unmeasured HREE.

## 5. Results

### 5.1. Petrography

#### 5.1.1. Jolotca hornblendite

The Jolotca hornblendites are coarse-grained rocks, characterised by hornblende, titanite, biotite (generally >0.5 mm), with minor plagioclase, apatite, and pyrite (Fig. 3(a)). Pál-Molnár et al. (2015a) provide a detailed petrographic description. Euhedral to subhedral hornblendes range from 0.5–7 mm in length, with some rims altered to biotite; smaller amphiboles (<1 mm) have internal zoning. Locally, hornblendes show a preferred alignment, defining a foliation. Interstitial plagioclase comprises <20% of the hornblendite. Unzoned apatites are euhedral to subhedral, with equant and acicular habits (<1 mm in length), they are referred to hereafter as $Ap_{JH}$, this corresponds to the apatite EPMA. Apatite inclusions are found in hornblende, plagioclase and euhedral titanite (1–2 mm). The Jolotca hornblendite is cut by thin (100–200 μm) carbonate and pyrite-dominated sulfide veins.

#### 5.1.2. Sărmaş gabbro

The Sărmaş gabbros are cumulate rocks of plagioclase, pyroxene, amphibole, biotite and titanite (Morogan et al., 2000; Pál-Molnár et al., 2015a). The gabbro has >60% mafic minerals and locally shows cumulus layering, alternating between mafic-rich and plagioclase-rich layers, 1–2 mm thick. Titanites, up to 1.5 mm, are common; they host ubiquitous apatite inclusions. Apatites and oxides (dominated by titanomagnetite) are common accessory minerals.

#### 5.1.3. Bear-valley mafic syenite

The Bear-valley mafic syenite comprises feldspar (perthitic microcline), <15% nepheline, amphibole and titanite (<5% of the rock). The mafic mineral phases are typically 0.3–1 mm diameter, while euhedral titanites and apatite are smaller (0.1–0.5 mm and < 0.1 mm respectively).

#### 5.1.4. Ditrău syenite

Across the complex, the Ditrău syenite varies from medium- to coarse-grained. Tabular feldspars, <2 mm in length, comprise >85% of the rock and c-axis alignment commonly defines a foliation. Orthoclase and microcline dominate with <10% plagioclase; the alkali feldspar grain boundaries are undulose. Ferromagnesian minerals comprise <10% of the total phases; subhedral amphiboles are the major mafic mineral. They are typically c. 0.5 mm across with associated biotite flakes up to 0.6 mm long. Accessory minerals (titanite, apatite and zircon) occur along alkali feldspar grain boundaries and as inclusions within the feldspars. Titanite is smaller (<0.6 mm) and less abundant than in the Jolotca hornblendite or Sărmaş gabbro. Zircons range from 0.3–0.5 mm. Alkali feldspars show limited alteration to sericite, which is generally constrained to the feldspar cores.

#### 5.1.5. Ghiduţ nepheline syenite

The Ghiduţ nepheline syenite is coarse-grained with large alkali feldspars and nephelines (Fig. 3(b)). Alkali feldspar (orthoclase, microcline and perthite) forms plates typically 2–3 mm (locally >5 mm), set in an alkali feldspar-rich groundmass. The alkali feldspars have undulose grain boundaries and no preferred orientation. Subhedral nepheline grains are up to 3 mm in diameter. Plagioclase laths (50–200 μm wide) are present in the groundmass and comprise <8% of the rock. Subhedral mafic phases include Na-pyroxenes (aegirine; c. 0.5 mm in diameter) and biotite (0.3–0.6 mm). Randomly oriented ultramafic clots (2 cm in diameter) are locally present. They are dominated by pyroxene, amphibole and biotite, with <10% leucocratic material.

Euhedral zircons, up to 3 mm in diameter, are common. The zircons have internal zoning and multiple inclusions; two zones are recognised: (1) an inclusion-free zone, commonly forming the core; and (2) a heterogeneous zone with multiple inclusions of varying sizes (<20–300 μm). This can be a single zircon or form an overgrowth rim around a type (1) zone. The type (2) zones host tabular albite inclusions (>50 μm long) that are continuous with the surrounding matrix and inclusions (typically <50 μm) of LREE, Y, Th- and/or Nb-bearing phases such as pyrochlore, thorite, zirconolite, and monazite.

Disseminated pyrites (0.2 mm wide) and a small amount of molybdenite are present throughout, but ilmenite and magnetite are the dominant oxides forming composite grains and ilmenite skeletal morphologies. Massive ilmenite reaches 0.6 mm. Ilmenite and rutile are associated with globular pyrochlore, which forms patches c. 0.2 mm wide, hosting Nb-Mn-Ti-rich inclusions. Accessory titanite (0.3–0.8 mm) is rarely present.

The lithology exhibits nepheline alteration, recrystallisation of feldspar, increased presence of perthite, and introduction of sodalite both

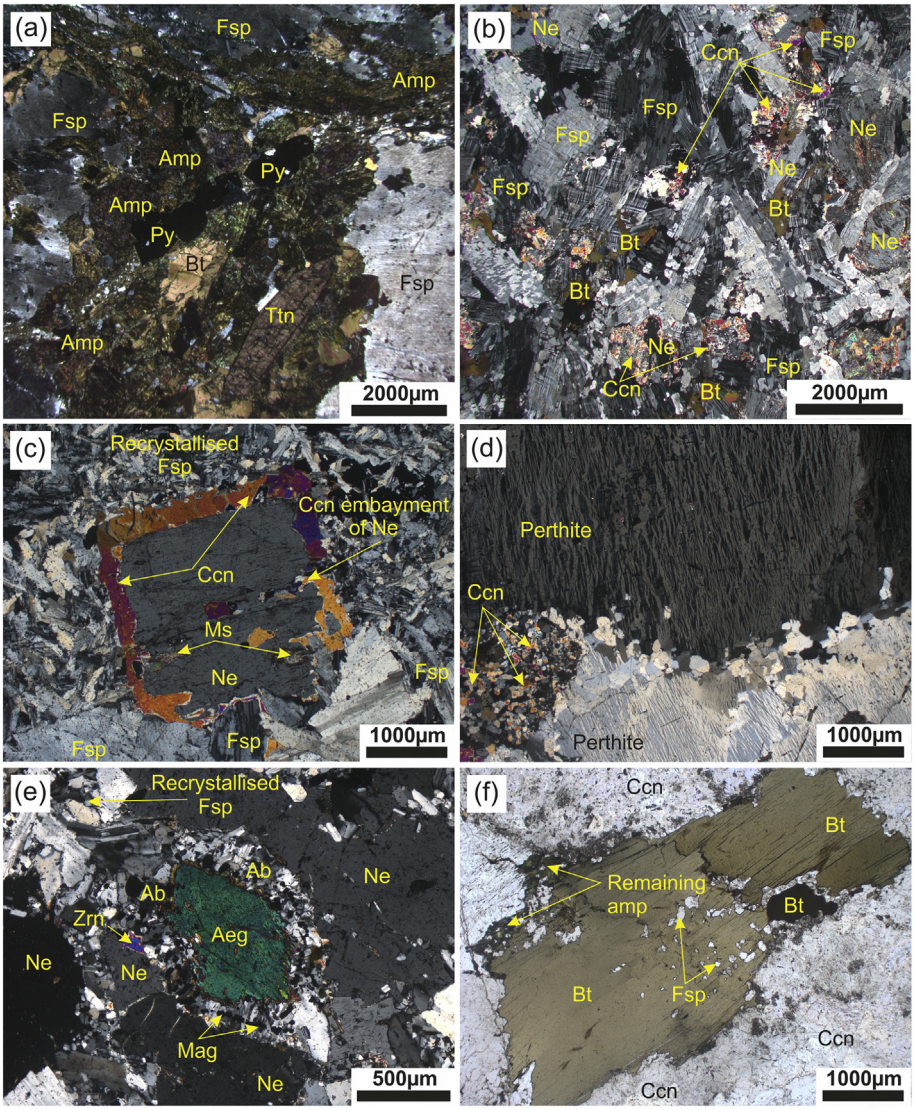


**Fig. 3.** (a) XPL photomicrograph of Jolotca hornblendite showing a titanite with apatite inclusions, associated with amphibole and biotite. (b) XPL overview of the Ghiduţ nepheline syenite showing alkali feldspars, nepheline, cancrinite and biotite. (c) XPL photomicrograph of nepheline alteration to cancrinite. (d) XPL photomicrograph of Ghiduţ nepheline syenite alteration, showing albitisation of perthite plates, with adjacent cancrinite. (e) Reaction texture, in XPL, between nepheline and aegirine. (f) XPL photomicrograph of Ghiduţ nepheline syenite alteration showing biotite with remaining traces of amphibole on the edge. Mineral abbreviations from Whitney and Evans (2010).

around nepheline rims and in fractures. This alteration is particularly evident in samples close to a biotite-rich mafic dyke.

Nepheline alteration in the Ghiduţ nepheline syenite is variable and can be separated into two phases. The first phase is alteration of nepheline to cancrinite, which forms stubby crystals that grow in from the margins of the nepheline (Fig. 3(c)). Sodalite, muscovite, pyrochlore, magnetite, and ilmenite occur between the cancrinite crystals. In places, cancrinite has replaced nepheline but not the alkali feldspar inclusions, as observed by Fall et al. (2007). The second phase comprises fine-grained muscovite aggregates replacing nepheline and cancrinite. Within the Ghiduţ nepheline syenite this alteration is poorly developed, occurring locally within nepheline cores. The two types of alteration can co-exist within a nepheline grain, with muscovite alteration more common in the core and cancrinite more common along the grain boundaries.

In samples close to a biotite-rich mafic dyke there is significant alteration of the nepheline syenite; larger alkali feldspars have rims recrystallised to albite and development of patchy perthite textures (Fig. 3(d)).

Alteration textures around Na-pyroxenes (aegirine) are common (Fig. 3(e)), and described in detail by Batki et al. (2018). Aegirines in proximity to nepheline (<1 mm) have a corona composed of: albite laths (0.2–0.3 mm), a band of magnetite (50 μm wide), small (<10 μm) inclusions of thorite, anhedral orthoclase, and pyrochlore crystals (50–100 μm wide). Between nepheline and albite laths there is a thin rim (<50 μm thick), which is low in K and Si, but enriched in Na and Ca.

The most altered samples contain large biotites, 1–3 mm, (Fig. 3(f)) and nepheline has been altered to micaceous aggregates and/or cancrinite, similar to textures seen in the LANS (see below).

*5.1.6. Lăzarea altered nepheline syenite (LANS)*

The LANS is medium- to coarse-grained, with variation in grain size between localities. The characteristic feature is complete alteration of primary nepheline (<5 mm diameter) to micaceous aggregates (i.e. liebnerite; Constantinescu and Anastasiu (1979); Fig. 4(a)). Perthitic alkali feldspar, up to 3 mm long, is a major phase and is locally sericitised and recrystallised. The main mafic minerals are amphibole and chloritised biotite, which typically form mafic clots 1–2 mm across, and comprise <10% of the rock. The mafic clots commonly contain apatite, titanite, sulfide, zircon, epidote group minerals and carbonate minerals. Pyrite (20 μm) and apatite grains (20–150 μm) vary in crystal

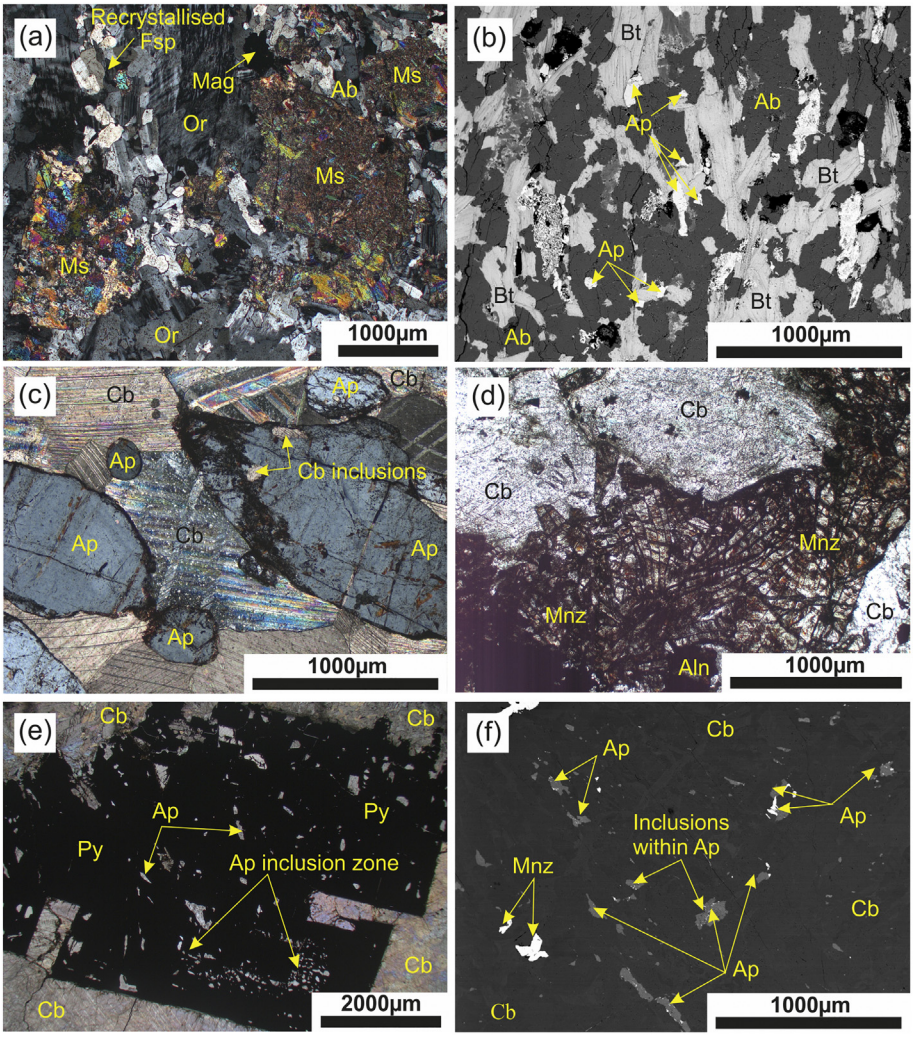


**Fig. 4.** (a) The Lăzarea altered nepheline syenite (LANS) in XPL, with muscovite pseudomorphs of nepheline. (b) Apatite in a biotite-rich vein, cutting the LANS, BSE image. (c) Apatite in a carbonate vein cutting the LANS, XPL image. (d) PPL photomicrograph of monazite laths surrounded by carbonate gangue within the mineralised veins. (e) BSE image of apatite inclusions in pyrite within the mineralised veins. (f) BSE image of apatite in the carbonate gangue of the mineralised veins. Mineral abbreviations from Whitney and Evans (2010).

shape and are disseminated through the LANS, they are named $Ap_{LANS}$. Subhedral zircons, generally <0.4 mm diameter, occur along feldspar grain boundaries. More typically zircons are found in fracture infills, which are pervasive in the LANS. Up to 1 mm wide, the fractures also host monazite, pyrochlore (<100 μm), magnetite, allanite and LREE carbonates (e.g. bastnäsite). The zircons have variable morphologies with thorite inclusions spread throughout and Ca-rich inclusions confined to the rims. Overall, HFSE-bearing accessory minerals are more abundant in the LANS than in other lithologies.

A variety of veins cross-cut the LANS, including aplitic syenite, biotite-rich, pyrite and carbonate veins. Aplitic syenite veins (0.5–5 cm wide) are dominated by fine-grained albite and orthoclase, and have accessory subhedral apatite crystals, varying from 20 to 100 μm ($Ap_{APLITIC}$). The apatites occur along albite and orthoclase grain boundaries, as inclusions in albite, along the margins of mafic clots and altered nephelines within the aplitic vein.

Biotite-rich veins, up to 1 cm wide, are comprised of subhedral biotite and albite laths (<0.5 mm), which make-up >85% of the vein. Biotite defines a foliation parallel with the vein margin (Fig. 4(b)). Accessory phases include euhedral–subhedral apatite (50–200 μm), titanite, titanomagnetite and muscovite. Apatite ($Ap_{BV}$) comprises c. 8% of the biotite-rich vein and occurs at albite and biotite boundaries, with the c-axis aligned with the foliation. There are rare apatite inclusions within biotite. Towards the vein margins the accessory phases decrease in size and abundance, and biotite becomes increasingly anhedral. Occasional zircon grains are associated with the vein margins.

Pyrite veins with associated sphalerite vary from 0.1–2 cm wide. Unlike the mineralised veins of the Jolotca region, these do not have associated REE-phosphate mineralisation or carbonate gangue.

Carbonate veins (>10 cm in width) cut all other veins in the LANS. They comprise coarse-grained, equigranular (120° triple junctions) carbonate hosting subhedral apatites (<2 mm in diameter; $Ap_{CV}$). These grains have a bimodal size distribution but both small and large apatites cluster together, with their c-axis aligned parallel to the vein margin (Fig. 4(c)). There are carbonate inclusions (10–200 μm diameter) in the rims of some apatite grains and alteration of the rims is common. The smaller grains have more alteration. Zircon occurs along the margins of the carbonate veins.

### 5.1.7. Hagota quartz syenite

This is a medium-grained, equigranular rock, dominated by alkali feldspar and <10% plagioclase (0.3–0.8 mm in diameter). Rare larger grains (~1 mm) have a perthitic texture and some feldspars have undergone secondary alteration to sericite. Interstitial quartz grains, generally >0.5 mm diameter, comprise c. 15% of the phases. Anhedral altered

**Table 2**
Whole rock major and trace element data. Lăzarea altered nepheline syenite is abbreviated to LANS.

| Sample number | DJ01 | DL34 | DD30 | DD22 | DL32 | DJ44 | DD29 |
|---|---|---|---|---|---|---|---|
| Rock type | Jolotca hornblendite | Mafic dyke | Deformed Sărmaș gabbro | Ditrău syenite | Ditrău syenite | Ditrău syenite | Bear-valley maifc syenite |
| Majors | wt.% | wt.% | wt.% | wt.% | wt.% | wt.% | wt.% |
| $SiO_2$ | 39.88 | 49.53 | 50.61 | 61.3 | 62.2 | 60.24 | 52.14 |
| $TiO_2$ | 3.73 | 2.15 | 1.95 | 0.38 | 0.46 | 0.81 | 2.05 |
| $Al_2O_3$ | 16.93 | 18.75 | 18.36 | 18.28 | 19.32 | 19.14 | 20.21 |
| $Fe_2O_{3\ TOTAL}$ | 13.59 | 7.81 | 8.33 | 3.68 | 2.91 | 3.39 | 6.43 |
| MnO | 0.26 | 0.20 | 0.14 | 0.23 | 0.12 | 0.11 | 0.14 |
| MgO | 4.08 | 2.18 | 3.5 | 0.18 | 0.3 | 0.62 | 1.52 |
| CaO | 10.97 | 5.69 | 6.66 | 1.5 | 0.98 | 2.13 | 6.08 |
| $Na_2O$ | 3.17 | 6.76 | 5.79 | 6.44 | 6.94 | 6.54 | 5.81 |
| $K_2O$ | 1.94 | 3.97 | 1.86 | 6.42 | 5.7 | 5.19 | 2.71 |
| $P_2O_5$ | 1.74 | 0.63 | 0.49 | 0.03 | 0.06 | 0.12 | 0.4 |
| LOI | 1.94 | 1.29 | 1.04 | 1.18 | 0.44 | 0.55 | 1.02 |
| Total | 99.06 | 99.35 | 99.21 | 99.74 | 99.61 | 99.22 | 99.34 |
| Mg no. | 20.6 | 19.4 | 26.6 | 4.0 | 8.2 | 13.6 | 16.9 |
| $Na_2O + K_2O$ | 5.11 | 10.73 | 7.65 | 12.86 | 12.64 | 11.73 | 8.52 |
| Trace elements | ppm | ppm | ppm | ppm | ppm | ppm | ppm |
| Cs | 0.65 | 1.00 | 1.58 | 1.72 | 0.43 | 0.45 | 0.22 |
| Rb | 47.81 | 113.37 | 39.55 | 205.80 | 129.07 | 104.50 | 43.74 |
| Ba | 1179.05 | 1013.76 | 1165.20 | 21.31 | 614.40 | 1864.82 | 3150.79 |
| Th | 8.07 | 18.71 | 4.64 | 12.60 | 8.18 | 6.24 | 7.70 |
| U | 1.46 | 6.29 | 0.86 | 3.09 | 1.32 | 1.05 | 1.40 |
| Ta | 16.56 | 8.12 | 4.08 | 6.27 | 6.41 | 9.83 | 14.15 |
| Nb | 261.02 | 171.32 | 94.03 | 159.37 | 127.55 | 142.65 | 250.90 |
| Mo | 3.83 | 4.04 | 1.22 | 5.82 | 0.43 | 0.70 | 3.75 |
| La | 193.68 | 105.29 | 72.38 | 165.39 | 54.46 | 91.96 | 141.56 |
| Ce | 379.51 | 171.08 | 116.82 | 185.82 | 92.24 | 157.88 | 247.54 |
| Sr | 3938.04 | 1271.10 | 2242.44 | 25.36 | 329.52 | 747.45 | 3389.30 |
| Nd | 165.48 | 63.59 | 44.04 | 34.54 | 28.32 | 57.88 | 84.75 |
| Hf | 8.93 | 11.34 | 5.51 | 7.57 | 8.40 | 7.63 | 6.88 |
| Zr | 283.98 | 520.70 | 231.98 | 365.70 | 398.05 | 342.07 | 260.67 |
| Y | 66.09 | 29.37 | 20.14 | 13.37 | 17.33 | 27.60 | 36.21 |

| Sample number | DL36 | DL35 | DJ43 | DD25 | DD26 | DL33 |
|---|---|---|---|---|---|---|
| Rock type | Bear-valley maifc syenite | Ghiduț nepheline syenite | Ghiduț nepheline syenite | Ghiduț nepheline syenite | Ghiduț nepheline syenite (altered) | Ghiduț nepheline syenite |
| Majors | wt.% | wt.% | wt.% | wt.% | wt.% | wt.% |
| $SiO_2$ | 51.37 | 59.16 | 61.99 | 57.75 | 56.17 | 57.23 |
| $TiO_2$ | 1.15 | 0.21 | 0.52 | 0.07 | 0.22 | 0.36 |
| $Al_2O_3$ | 21.23 | 21.34 | 20.16 | 22.51 | 22.19 | 21.46 |
| $Fe_2O_{3\ TOTAL}$ | 5.17 | 2.08 | 1.69 | 2.24 | 1.57 | 2.48 |
| MnO | 0.20 | 0.07 | 0.03 | 0.06 | 0.07 | 0.13 |
| MgO | 0.85 | 0.22 | 0.42 | *0.05* | 0.49 | 0.2 |
| CaO | 3.8 | 0.61 | 2.35 | 0.32 | 1.37 | 1.39 |
| $Na_2O$ | 8.47 | 8.54 | 7.31 | 12.81 | 12.94 | 8.41 |
| $K_2O$ | 4.65 | 6.29 | 4.18 | 2.55 | 0.72 | 6.1 |
| $P_2O_5$ | 0.2 | 0.03 | 0.09 | <0.01 | <0.01 | 0.04 |
| LOI | 1.92 | 1.23 | 0.35 | 1.16 | 3.6 | 1.3 |
| Total | 99.5 | 99.83 | 99.85 | 99.67 | 99.89 | 99.2 |
| Mg no. | 12.4 | 8.4 | 17.6 | 1.9 | 21.2 | 6.5 |
| $Na_2O + K_2O$ | 13.12 | 14.83 | 11.49 | 15.36 | 13.66 | 14.51 |
| Trace elements | ppm | ppm | ppm | ppm | ppm | ppm |
| Cs | 1.09 | 1.02 | 0.52 | 0.62 | 2.26 | 0.67 |
| Rb | 107.53 | 288.80 | 64.63 | 84.04 | 44.37 | 184.83 |
| Ba | 1878.02 | 194.39 | 2958.91 | 109.99 | 194.85 | 230.89 |
| Th | 21.60 | 5.99 | 5.97 | 72.45 | 3.48 | 4.49 |
| U | 2.58 | 1.75 | 1.40 | 33.80 | 3.08 | 0.87 |
| Ta | 9.15 | 0.73 | 3.73 | 19.71 | 0.69 | 2.44 |
| Nb | 264.92 | 17.60 | 74.82 | 609.99 | 46.41 | 81.54 |
| Mo | 1.43 | 0.45 | 0.61 | 0.71 | 1.98 | 0.61 |
| La | 113.26 | 17.63 | 50.93 | 32.22 | 27.22 | 43.07 |
| Ce | 180.94 | 22.12 | 76.58 | 71.00 | 36.28 | 64.19 |
| Sr | 1444.63 | 170.91 | 1568.96 | 98.82 | 1010.28 | 194.16 |
| Nd | 52.83 | 5.47 | 25.32 | 19.28 | 10.31 | 14.19 |
| Hf | 9.91 | 1.63 | 18.96 | 20.48 | 0.20 | 5.92 |
| Zr | 484.44 | 68.54 | 1310.23 | 961.90 | 2.59 | 295.23 |
| Y | 28.60 | 3.00 | 13.23 | 13.78 | 2.60 | 10.89 |

**Table 2** (*continued*)

| Sample number | DL09 | DL11 | DL19 | DL21 | DD24 | DD46 | DD45 |
|---|---|---|---|---|---|---|---|
| Rock type | LANS | LANS | LANS | LANS | LANS (most enriched) | LANS | Hagota quartz syenite |
| Majors | wt.% | wt.% | wt.% | wt.% | wt.% | wt.% | wt.% |
| $SiO_2$ | 59.22 | 61.79 | 60.19 | 61.48 | 59.5 | 58.17 | 66.29 |
| $TiO_2$ | 0.23 | 0.34 | 0.18 | 0.3 | 0.17 | 0.64 | 0.44 |
| $Al_2O_3$ | 22.45 | 18.36 | 22.56 | 20.64 | 23.12 | 20 | 16.48 |
| $Fe_2O_{3\ TOTAL}$ | 2.91 | 2.33 | 1.32 | 2.64 | 1.7 | 3.07 | 2.49 |
| MnO | 0.11 | 0.14 | 0.05 | 0.04 | <0.01 | 0.11 | 0.07 |
| MgO | 0.38 | 0.17 | 0.21 | 0.45 | 0.12 | 1.06 | 0.32 |
| CaO | 0.11 | 1.68 | 0.08 | 0.14 | 0.06 | 1.25 | 0.65 |
| $Na_2O$ | 5.19 | 6.52 | 5.3 | 5.68 | 6.53 | 5.17 | 6.03 |
| $K_2O$ | 7.48 | 6.47 | 7.64 | 7.34 | 5.75 | 6.81 | 5.75 |
| $P_2O_5$ | 0.02 | 0.04 | 0.02 | 0.04 | <0.01 | 0.06 | 0.06 |
| LOI | 1.27 | 1.34 | 1.45 | 1.09 | 1.92 | 2.43 | 0.38 |
| Total | 99.71 | 99.47 | 99.07 | 99.94 | 99.22 | 99.09 | 99.08 |
| Mg no. | 10.1 | 5.9 | 12.1 | 12.8 | 5.7 | 22.9 | 10.0 |
| $Na_2O + K_2O$ | 12.67 | 12.99 | 12.94 | 13.02 | 12.28 | 11.98 | 11.78 |
| Trace elements | ppm | ppm | ppm | ppm | ppm | ppm | ppm |
| Cs | 0.59 | 0.93 | 0.31 | 0.59 | 0.38 | 4.45 | 1.34 |
| Rb | 278.54 | 160.49 | 272.78 | 227.46 | 254.54 | 224.68 | 215.56 |
| Ba | 518.97 | 585.37 | 227.88 | 378.84 | 211.93 | 1328.03 | 392.76 |
| Th | 52.09 | 19.44 | 8.51 | 12.89 | 11.69 | 25.50 | 27.34 |
| U | 7.67 | 3.42 | 1.49 | 7.12 | 12.42 | 4.38 | 4.87 |
| Ta | 5.77 | 4.19 | 3.27 | 8.44 | 3.33 | 4.59 | 8.79 |
| Nb | 302.27 | 115.95 | 85.74 | 200.01 | 306.54 | 154.20 | 137.28 |
| Mo | 0.28 | 0.12 | 0.26 | 0.42 | 11.69 | 1.20 | 0.52 |
| La | 22.61 | 64.59 | 25.24 | 41.06 | 23.41 | 105.64 | 53.34 |
| Ce | 28.56 | 86.11 | 35.91 | 72.74 | 22.35 | 120.06 | 99.25 |
| Sr | 306.82 | 342.90 | 131.11 | 273.95 | 25.81 | 765.26 | 154.60 |
| Nd | 7.23 | 20.03 | 9.80 | 20.20 | 3.14 | 32.80 | 36.11 |
| Hf | 22.10 | 14.14 | 5.33 | 4.79 | 22.42 | 7.98 | 10.99 |
| Zr | 1174.91 | 924.33 | 256.76 | 178.15 | 1593.87 | 448.65 | 472.15 |
| Y | 4.88 | 13.07 | 5.48 | 8.76 | 7.91 | 18.94 | 28.67 |

amphibole has <7% modal abundance and is associated with rare anhedral biotite and occasional titanite grains (<200 μm wide). Small zircons (0.2–0.5 mm in width) occur along feldspar and quartz grain boundaries.

#### 5.1.8. Mafic dykes

The mafic dykes are fine-grained (50–300 μm) and generally equigranular. They are typically lamprophyres as described by Batki et al. (2014), with >60% mafic phases (chiefly pyroxenes and amphiboles), and euhedral titanite. There are rare instances of large, inclusion-bearing amphiboles (>500 μm in width) and large titanites (>400 μm). Feldspars and feldspathoids are present, with small areas altered to sericite and cancrinite. There is a weak foliation, defined by c-axis alignment of the biotite. Alteration of the mafic dykes made them extremely friable, so it is not possible to give a petrographic description of the altered mafic dykes.

#### 5.1.9. Mineralised veins

The Jolotca mineralised veins are dominated by monazite (a key REE ore mineral at Ditrău), with varying amounts of allanite, bastnäsite, rutile, molybdenite and sulfides (chiefly pyrite); these are hosted in a carbonate gangue. Other minerals have previously been recognised in these veins, including: chevkinite, cerite, columbite, euxenite, aeschynite, parisite, synchysite and thorite (Hirtopanu et al., 2010, 2013a, 2015). Large (0.1–1 cm diameter) aggregates of monazite (Fig. 4(d)) host inclusions of thorite and zirconolite. Interstitial molybdenite lies between the monazite laths. The monazite aggregates are adjacent to massive pyrite (>3 mm), sphalerite (<2 mm) and galena (<1 mm). The pyrite hosts numerous apatite inclusions (100–500 μm; $Ap_{PY}$). Inclusions of monazite (c. 0.2 mm long) are concentrated along the pyrite margins and inclusions of carbonate, galena and chalcopyrite lie within the outer zone of the pyrite rim (Fig. 4(e)). Sphalerite contains small inclusions of galena and pyrite (<50 μm).

LREE carbonates, phosphates and silicates (e.g. allanite, apatite, and chlorite) are associated with the grain boundaries of monazite (Hirtopanu et al., 2010), particularly adjacent to fine-grained calcite. Allanite also forms thin veins (c. 100 μm wide) cutting across the monazite aggregates. There are three distinct apatite populations in the mineralised veins: (1) apatite associated with allanite ($Ap_{ALN}$); (2) apatite associated with pyrite ($Ap_{PY}$); and (3) apatite (<300 μm diameter) distributed throughout the carbonate gangue ($Ap_{MV}$; Fig. 4(f)). The apatite inclusions within the large pyrite grains form distinct zones. The grains nearest the pyrite rim are globular and inclusion-free, whereas $Ap_{PY}$ nearer the core of the pyrite grain, themselves, contain REE-enriched inclusions; these are typically elongated parallel to the apatite c-axis. Inclusions within $Ap_{MV}$ are rare, but where present, they are LREE-enriched. REE-bearing inclusions were not found in $Ap_{ALN}$.

Two carbonate gangue phases are recognised in the mineralised veins: (1) fine-grained (<50 μm) calcite containing laths of monazite, pyrite, apatite, allanite, rutile and bastnäsite (Fig. 4(f)). Ferrodolomite, ankerite and siderite have previously been identified (Hirtopanu et al., 2013a); and (2) a coarse-grained calcite, with 120° internal grain boundary angles. Type (2) forms multiple veinlets (0.5–3 mm wide) with sharp boundaries against type (1), and cuts all other phases within the mineralised veins.

### 5.2. Whole rock geochemistry

Major and trace element data for the lithologies are in Table 2. $SiO_2$ ranges from 39.88–66.29 wt.% and $Fe_2O_{3\ total}$, MnO, $TiO_2$, MgO, and CaO have a negative correlation with $SiO_2$ (Fig. 5(a–e)). Total $Fe_2O_3$ reaches a maximum of 13.59 wt.% in the Jolotca hornblendite, and is lowest in the syenites (c. 2 wt.%). Similarly, the Jolotca hornblendite, Sărmaş gabbro and Bear-valley mafic syenite have elevated $TiO_2$ concentrations, up to 3.73 wt.%, while the syenitic rocks contain <0.64 wt.%. Magnesium numbers (calculated as 100 (Mg/(Mg + Fe))) range

from 27 for the deformed Sărmaş gabbro to 2 for the Ghiduţ nepheline syenite. CaO is highest in the mafic lithologies, up to 10.97 wt.% in the Jolotca hornblendites; for the felsic lithologies CaO is typically below 3 wt.%, with negligible concentrations in the LANS.

$K_2O$ concentrations show an overall weak positive correlation with $SiO_2$, ranging from 1.94 wt.% in the Jolotca hornblendite to a maximum of 7.64 wt.% in the LANS. The Ghiduţ nepheline syenite samples have a wide range of $K_2O$ values (2.55–6.24 wt.%). The altered Ghiduţ

**Table 3**
Whole rock REE element data. Lăzarea altered nepheline syenite is abbreviated to LANS.

| Sample number | DJ01 | DL34 | DD30 | DD22 | DL32 | DJ44 | DD29 |
|---|---|---|---|---|---|---|---|
| Rock type | Jolotca hornblendite | Mafic dyke | Deformed Sărmaş gabbro | Ditrău syenite | Ditrău syenite | Ditrău syenite | Bear-valley mafic syenite |
| REE | ppm | ppm | ppm | ppm | ppm | ppm | ppm |
| La | 193.68 | 105.29 | 72.38 | 165.39 | 54.46 | 91.96 | 141.56 |
| Ce | 379.51 | 171.08 | 116.82 | 185.82 | 92.24 | 157.88 | 247.54 |
| Pr | 44.13 | 17.83 | 12.30 | 13.78 | 9.75 | 16.86 | 25.70 |
| Nd | 165.48 | 63.59 | 44.04 | 34.54 | 28.32 | 57.88 | 84.75 |
| Sm | 27.01 | 10.34 | 7.42 | 3.83 | 4.07 | 9.15 | 13.60 |
| Eu | 8.18 | 3.09 | 2.47 | 0.64 | 0.90 | 2.42 | 4.00 |
| Gd | 21.67 | 8.89 | 6.21 | 2.69 | 3.47 | 7.13 | 10.26 |
| Tb | 2.74 | 1.13 | 0.86 | 0.39 | 0.51 | 0.98 | 1.38 |
| Dy | 14.02 | 5.87 | 4.20 | 2.23 | 2.94 | 5.16 | 7.45 |
| Ho | 2.58 | 1.11 | 0.77 | 0.48 | 0.62 | 1.04 | 1.36 |
| Er | 6.03 | 2.76 | 1.81 | 1.37 | 1.68 | 2.61 | 3.43 |
| Tm | 0.82 | 0.39 | 0.29 | 0.24 | 0.28 | 0.39 | 0.47 |
| Yb | 4.31 | 2.32 | 1.53 | 1.66 | 1.70 | 2.14 | 2.62 |
| Lu | 0.59 | 0.34 | 0.26 | 0.31 | 0.26 | 0.30 | 0.36 |
| $REE_{TOTAL}$ | 870.75 | 394.02 | 271.35 | 413.37 | 201.21 | 355.88 | 544.49 |
| $(La/Lu)_N$ | 10 | 86 | 25 | 14 | 55 | 22 | 16 |

| Sample number | DL36 | DL35 | DJ43 | DD25 | DD26 | DL33 | DL09 |
|---|---|---|---|---|---|---|---|
| Rock type | Bear-valley maifc syenite | Ghiduţ nepheline syenite | Ghiduţ nepheline syenite | Ghiduţ nepheline syenite | Ghiduţ nepheline syenite (altered) | Ghiduţ nepheline syenite | LANS |
| REE | ppm | ppm | ppm | ppm | ppm | ppm | ppm |
| La | 113.26 | 17.63 | 50.93 | 32.22 | 27.22 | 43.07 | 22.61 |
| Ce | 180.94 | 22.12 | 76.58 | 71.00 | 36.28 | 64.19 | 28.56 |
| Pr | 17.12 | 1.87 | 7.57 | 6.55 | 3.52 | 5.41 | 2.57 |
| Nd | 52.83 | 5.47 | 25.32 | 19.28 | 10.31 | 14.19 | 7.23 |
| Sm | 7.65 | 0.78 | 3.81 | 2.60 | 1.45 | 2.03 | 1.09 |
| Eu | 2.41 | 0.25 | 1.37 | 0.71 | 0.38 | 0.56 | 0.28 |
| Gd | 6.16 | 0.65 | 3.17 | 2.13 | 0.95 | 1.77 | 0.83 |
| Tb | 0.91 | 0.10 | 0.44 | 0.34 | 0.12 | 0.26 | 0.13 |
| Dy | 4.94 | 0.52 | 2.44 | 2.11 | 0.51 | 1.58 | 0.77 |
| Ho | 1.03 | 0.12 | 0.47 | 0.51 | 0.10 | 0.40 | 0.20 |
| Er | 2.73 | 0.31 | 1.32 | 1.58 | 0.23 | 1.19 | 0.59 |
| Tm | 0.44 | 0.06 | 0.20 | 0.30 | 0.03 | 0.20 | 0.12 |
| Yb | 2.65 | 0.37 | 1.31 | 1.88 | 0.21 | 1.54 | 0.89 |
| Lu | 0.40 | 0.07 | 0.22 | 0.33 | 0.03 | 0.28 | 0.17 |
| $REE_{TOTAL}$ | 393.47 | 50.34 | 175.15 | 141.56 | 81.33 | 136.69 | 66.06 |
| $(La/Lu)_N$ | 32 | 18 | 22 | 31 | 7 | 24 | 40 |

| Sample number | DL11 | DL19 | DL21 | DD24 | DD46 | DD45 |
|---|---|---|---|---|---|---|
| Rock type | LANS | LANS | LANS | LANS (most enriched) | LANS | Hagota quartz syenite |
| REE | ppm | ppm | ppm | ppm | ppm | ppm |
| La | 64.59 | 25.24 | 41.06 | 23.41 | 105.64 | 53.34 |
| Ce | 86.11 | 35.91 | 72.74 | 22.35 | 120.06 | 99.25 |
| Pr | 7.17 | 3.49 | 6.87 | 1.33 | 11.54 | 10.71 |
| Nd | 20.03 | 9.80 | 20.20 | 3.14 | 32.80 | 36.11 |
| Sm | 2.45 | 1.45 | 2.81 | 0.56 | 4.15 | 6.42 |
| Eu | 0.53 | 0.29 | 0.53 | 0.21 | 1.22 | 0.91 |
| Gd | 2.01 | 1.16 | 2.32 | 0.67 | 3.19 | 5.42 |
| Tb | 0.29 | 0.17 | 0.32 | 0.13 | 0.44 | 0.83 |
| Dy | 1.86 | 0.95 | 1.79 | 0.97 | 2.57 | 4.83 |
| Ho | 0.44 | 0.21 | 0.35 | 0.27 | 0.57 | 0.98 |
| Er | 1.38 | 0.62 | 0.99 | 1.09 | 1.71 | 2.68 |
| Tm | 0.26 | 0.11 | 0.14 | 0.25 | 0.29 | 0.45 |
| Yb | 1.97 | 0.74 | 0.89 | 1.85 | 1.90 | 2.73 |
| Lu | 0.37 | 0.12 | 0.14 | 0.36 | 0.28 | 0.42 |
| $REE_{TOTAL}$ | 189.47 | 80.27 | 151.14 | 56.60 | 286.36 | 225.08 |
| $(La/Lu)_N$ | 29 | 34 | 41 | 29 | 32 | 13 |

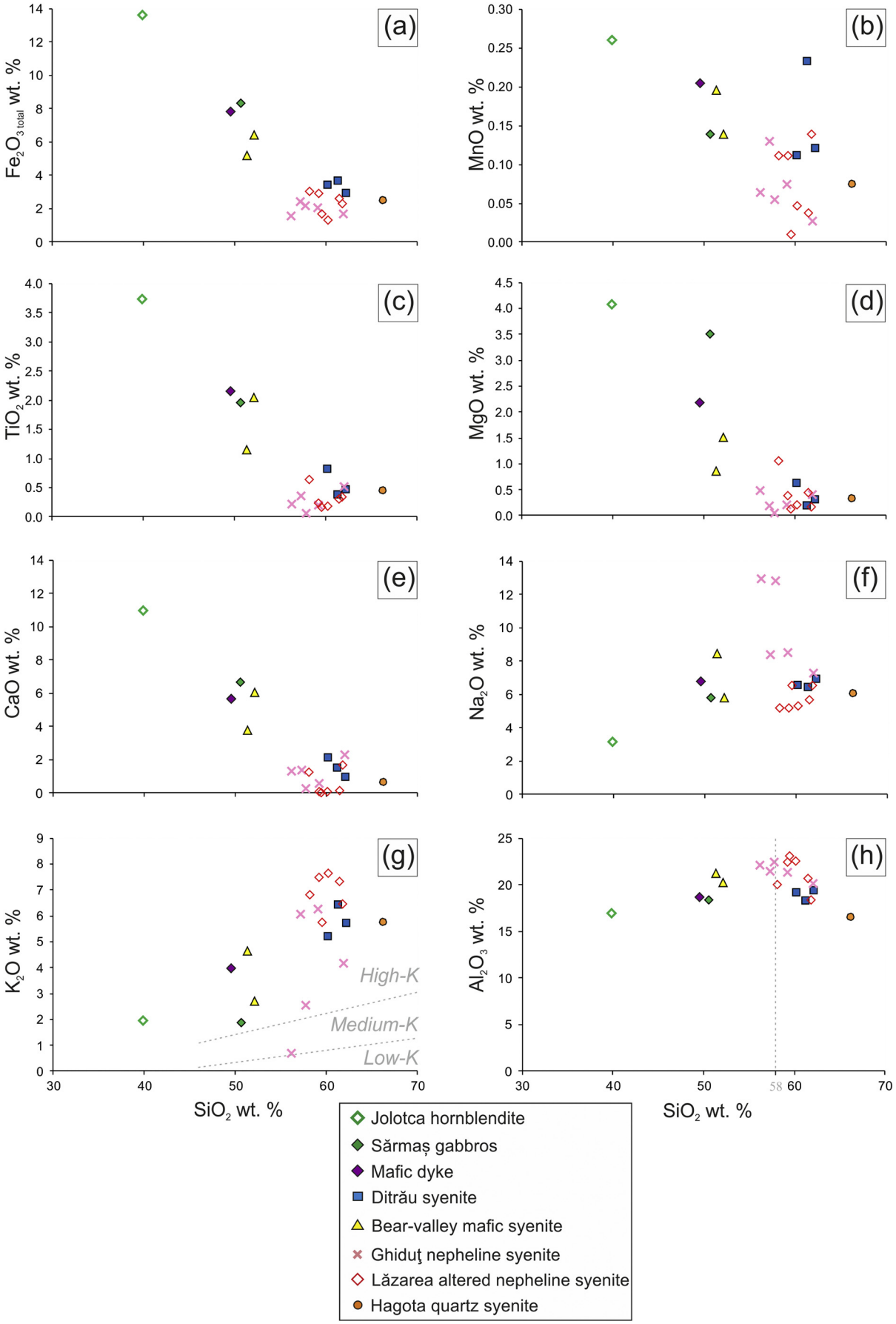


**Fig. 5.** Harker plots for the Ditrău Complex.

nepheline syenite adjacent to a mafic dyke has a lower $K_2O$ concentration (0.72 wt.%), and the mafic dyke has a $K_2O$ concentration of 3.97 wt.%.

$Na_2O$ concentrations correlate positively with $SiO_2$ up to 55 wt.%, above this concentration there is a divergence from a single trend (Fig. 5(f)) and the syenites have a negative correlation between $K_2O$ and $Na_2O$ concentrations (Fig. 6). The Ghiduţ nepheline syenite has high $Na_2O$ (7.31–12.94 wt.%), whereas the LANS has lower $Na_2O$ values of 5.17–6.53 wt.%.

$Al_2O_3$ values are high across the complex, ranging from 17 wt.% in the Hagota quartz syenite to 23 wt.% in the Ghiduţ nepheline syenite. These values are comparable to previously published data for the Ditrău Complex (Morogan et al., 2000). The Harker plot for $Al_2O_3$ has a concave trend, with an inflection at 58 wt.% $SiO_2$, correlating with the appearance of alkali feldspar (Fig. 5(h)).

Total alkali contents ($Na_2O + K_2O$), are generally high (between 5.11 and 15.36 wt.%; Table 2). The lithology with the lowest total alkalis is the Jolotca hornblendite (Fig. 7). The Ghiduţ nepheline syenite lies within the nepheline syenite field, whereas the LANS and Ditrău syenite plot along the nepheline syenite–syenite boundary with similar $SiO_2$ values and total alkali contents (c. 12 wt.%). The total alkali-silica plot has a split trend at higher $SiO_2$ with more Na-rich and K-rich lithologies (Fig. 7).

Zr and $SiO_2$ show no significant correlation (Fig. 8). In primitive mantle normalised trace element plots (Fig. 9(a)), the mafic lithologies have trace element patterns similar to Ocean Island Basalts (OIB), being enriched in high field strength elements (HFSE). The Jolotca hornblendite and Sărmaş gabbro have high concentrations of Ta and Nb. The Ditrău syenite and Hagota quartz syenite have relatively high concentrations of Rb, K, Hf and Zr but are depleted in Ba and Sr. The Hagota quartz syenite also shows notable enrichment in Th and U compared to the more mafic lithologies.

The Ghiduţ nepheline syenite adjacent to a mafic dyke is altered and in comparison to the Ghiduţ nepheline syenite, it is depleted in the HFSE (Fig. 9(b)). The mafic dyke has a relatively flat trace element pattern with concentrations of the HFSE comparable to the mafic lithologies. The LANS samples are enriched in HFSE (Fig. 9(b)). The sample with a strong positive Nb anomaly, has a large amount of pyrochlore in hand specimen. The LANS is typically depleted in Cs, Ba and Sr.

All magmatic lithologies of the Ditrău Complex are relatively light rare earth element (LREE) enriched and typically lack Eu anomalies (Fig. 10; Table 3). The $(La/Lu)_N$ ratio varies widely, from 13 for the Hagota quartz syenite to 34 for the Jolotca hornblendite. The mafic lithologies have the highest total REE concentrations, reaching 871 ppm for the Jolotca hornblendite and 544 ppm for the Sărmaş gabbro. The known REE-bearing phases in these lithologies are cumulus titanite (Morogan et al., 2000) and apatite. The lithologies with high $TiO_2$ are enriched in REE. A mafic dyke in the Ghiduţ nepheline syenite has a relative enrichment in REE compared to the syenites; the concentrations are similar to the Jolotca hornblendite. The Hagota quartz syenite has a minor negative Eu anomaly ($Eu/Eu^* = 0.47$). The Ghiduţ nepheline syenites and the LANS have relatively low REE concentrations; some LANS samples have a weakly concave pattern, with higher normalised concentrations of HREE. Higher concentrations of HREE in the LANS relative to the Ghiduţ nepheline syenite correlate with zircon abundance. The depletion of the middle rare earth elements (MREE) is most pronounced in samples of LANS and altered Ghiduţ nepheline syenite. These altered lithologies are also depleted in the LREE relative to the other syenitic lithologies.

The mineralised veins have not been analysed for whole-rock geochemistry, since their mineralogy is too heterogeneous to obtain a representative sample. Săbău (2015, pers. comm.) documents two generations of monazite based on the thorium content: (1) an early phase of Th-poor monazite and, (2) a later (main) Th-rich monazite. From XRF analysis in the field and EDS SEM analysis, only the Th-rich type was collected in this study.

### 5.3. Apatite mineral chemistry

Apatite grains from eight samples were analysed by EPMA, to investigate variations in REE concentration; apatite in six of the samples has total REE >1 wt.%. The analysed samples are representative of apatite from the Jolotca hornblendite, the LANS, and the mineralised veins in the Jolotca region, Table 4 details the abbreviations used. The LANS is cut by aplitic syenite, biotite and carbonate veins; apatite grains from these were analysed. Data is presented in Supplementary Table 2.

#### 5.3.1. Apatite volatile contents

The F content of the Ditrău apatite varies between 2.30 and 4.92 wt.%, while the Cl content is typically below 0.32 wt.%. Samples collected during this study contain no chlorapatite (based on apatites analysed); this is in agreement with observations by Piccoli and Candela (2002) that chlorapatite is generally rare. Stoichiometric fluorapatite can contain a maximum of 3.76 wt.% F (Pyle et al., 2002); therefore the apatite crystals from this study with F concentrations >3.76 wt.% are classified as end-member fluorapatite within analytical uncertainty, as the excess F is likely due to electron beam induced F migration (Stock et al., 2015). The LANS, and associated veins are dominated by end-member fluorapatite.

#### 5.3.2. Jolotca hornblendite

The apatite within the Jolotca hornblendite ($Ap_{JH}$) has the highest Cl concentration relative to the other apatites, with a maximum value of 0.32 ± 0.06 wt.%. $Ap_{JH}$ have the lowest total REE (TREE + Y) content of all analysed apatites, with a maximum Ce value of 0.27 wt.% ± 0.02, and an average of 0.10 wt.%. The maximum Y value is 0.03 ± 0.02 wt.%. The variability between each apatite REE pattern is low. The REE pattern is enriched in LREE, decreasing linearly with a shallow gradient to Y (Fig. 11(a)), as is typical of magmatic apatite analysed in intrusions (e.g. Rønsbo, 2008; Vantongeren and Mathez, 2012).

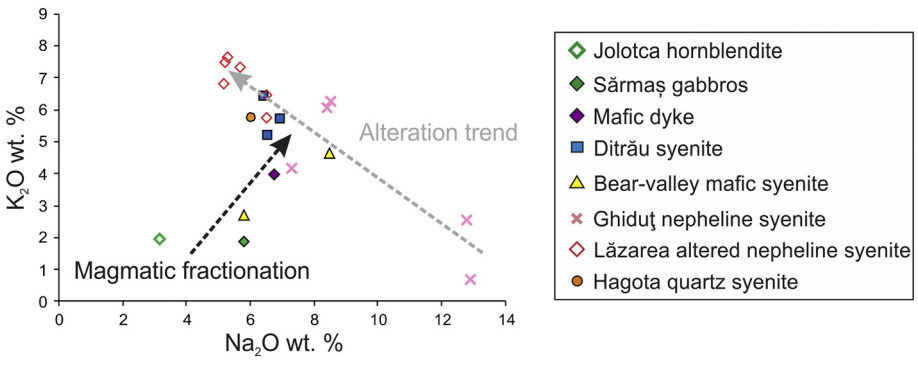


**Fig. 6.** Plot of $Na_2O$ wt.% against $K_2O$ wt.%. The black arrow shows the magmatic fractionation trend, the grey arrow shows the alteration trend of the syenites.

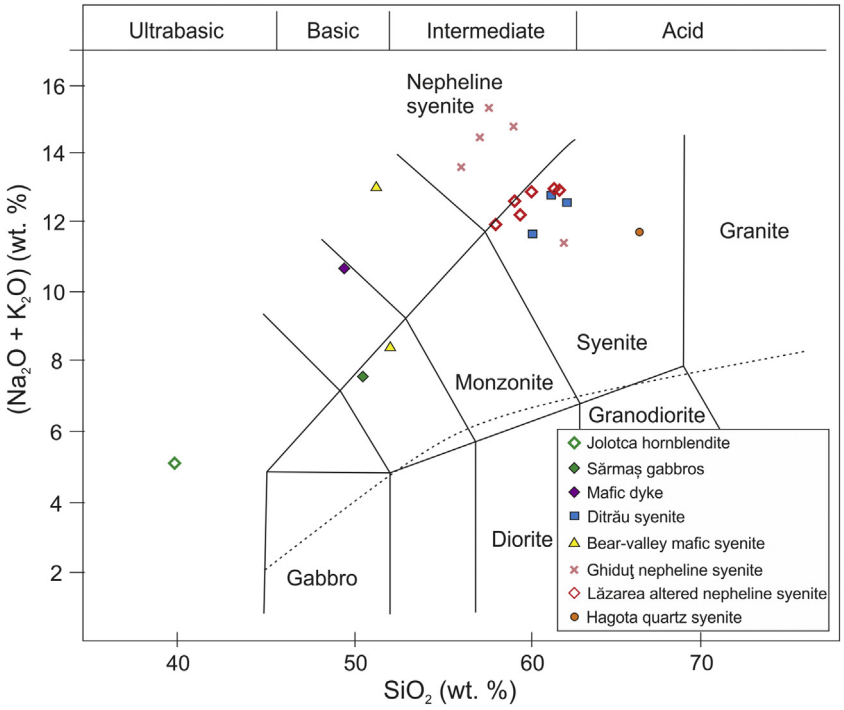


**Fig. 7.** Plot of total alkalis versus silica for the sampled lithologies of the Ditrău Complex. Fields from Gillespie and Styles (1999). Dashed line represents boundary between alkalic rocks (above) and subalkalic rocks below (Miyashiro, 1974).

*5.3.3. Lăzarea altered nepheline syenite (LANS)*

Apatites within the LANS are LREE-enriched with low Y concentrations, forming a linear pattern (Fig. 11 (b, c)). $Ap_{LANS}$ crystallised within the body of the LANS and has a Ce maximum concentration of 2.28 ± 0.04 wt.%, a La maximum of 1.41 ± 0.04 wt.% and a Y maximum of 0.84 ± 0.02 wt.%. Apatite from samples near the margins of the LANS typically have lower TREE + Y concentrations (Supplementary Table 2).

*5.3.3.1. Aplitic syenite vein cutting the LANS.* The aplitic syenite vein apatite ($Ap_{APLITIC}$) is the most LREE-enriched in the complex (Fig. 11(d)). $Ap_{APLITIC}$ TREE + Y concentrations range from 1.18–7.01 wt.%, despite the variability, there is no obvious correlation between the apatite location and REE content. Ce is the dominant REE with an average concentration of 1.83 wt.% and a maximum of 3.39 ± 0.06 wt.%, followed by La with an average of 1.21 wt.% and maximum of 2.37 ± 0.06 wt.%. Nd has a maximum concentration of 0.74 ± 0.06 wt.%, whereas Y has an average concentration of 0.23 wt.% and a maximum of 0.38 ± 0.02 wt.%; this forms the typical Ditrău REE pattern of a downward linear slope.

*5.3.3.2. Biotite-rich vein cutting the LANS.* The apatite in the biotite-rich vein ($Ap_{BV}$) is LREE dominated with minimal variability in TREE + Y concentration (Fig. 11(e)). Only apatite grains from the vein centre were large enough for EPMA. The maximum La concentration is 0.40 ± 0.02 wt.% with an average of 0.28 wt.%. The average Nd and Y concentrations are 0.14 wt.% and 0.07 wt.% respectively, forming a linear LREE-enriched pattern.

*5.3.3.3. Carbonate vein cutting the LANS.* The apatites within the carbonate vein cutting the LANS are LREE-dominated, forming two distinct apatite populations of: (1) small REE-enriched apatites, $Ap_{CV(S)}$ and (2) large REE-depleted apatites $Ap_{CV(L)}$ (Fig. 11(f)). The Ce range in the REE-enriched group is 1.92–2.59 wt.% and 0.64–1.07 wt.% in the REE-depleted group. The maximum value for Y within the REE-enriched group is 0.25 ± 0.02 wt.% whereas in the REE-depleted group it is 0.12 ±

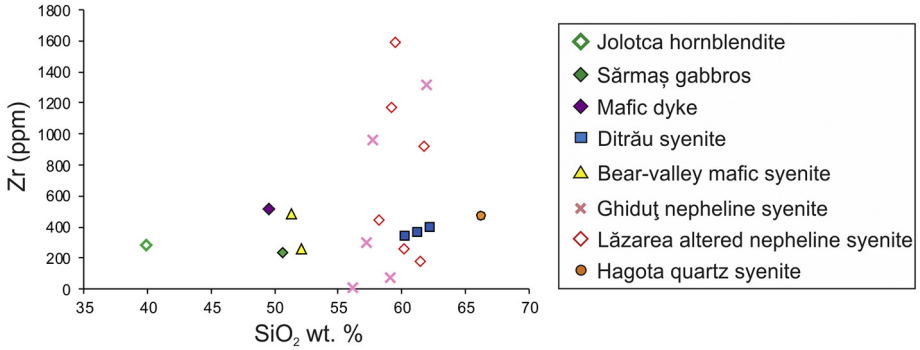


**Fig. 8.** Plot of $SiO_2$ wt.% against Zr (ppm) for the Ditrău Complex.

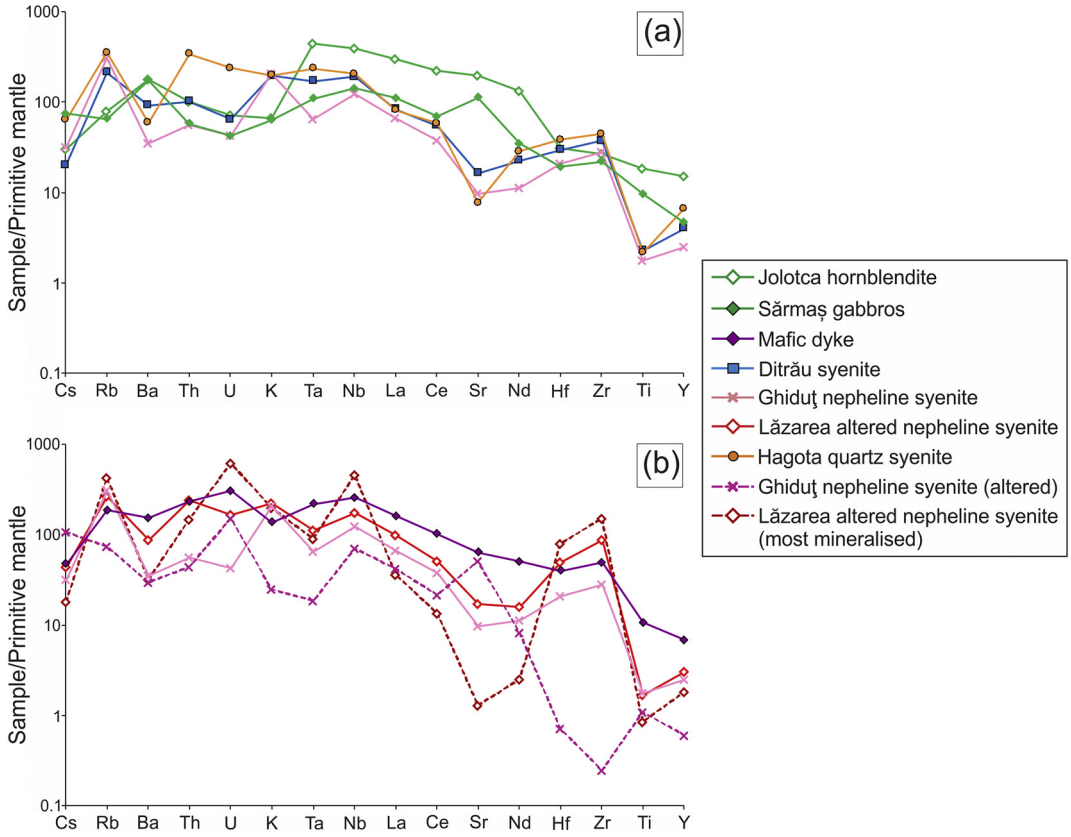


**Fig. 9.** Primitive-mantle normalised spider diagram for representative samples of different lithologies within the Ditrău Complex. Normalising values from McDonough and Sun (1995). (a) Magmatic lithologies. (b) Altered and magmatic lithologies.

0.02 wt.%. The REE pattern is a linear declining trend, from high LREE to low Y; this pattern is the same for both apatite groups. Apatite grains with altered rims are common, typically these are enriched in REE + Y compared to the apatite cores. The altered rims have higher $Na_2O$ and $SiO_2$ and lower CaO concentrations. REE compositional profiles are relatively flat across unaltered apatite grains suggesting minimal magmatic chemical zonation.

*5.3.4. Mineralised veins*

The mineralised veins have three populations of apatite: (1) apatite inclusions in, or along the margins of allanite ($Ap_{ALN}$; Fig. 11(g)); (2) apatite trapped as inclusions within pyrite grains ($Ap_{PY}$; Fig. 11(h)); and (3) apatite hosted in carbonate gangue ($Ap_{MV}$; Fig. 11(h)).

The apatite REE pattern of the mineralised vein is distinctly different to the linear LREE enriched patterns of apatites in the other lithologies. The pattern is a flattened convex with a curved increase from La to Nd, then a plateau or small decrease to Y.

The apatites associated with allanite ($Ap_{ALN}$) have the lowest TREE + Y concentrations averaging 0.24 wt.%. The carbonate gangue hosted apatites ($Ap_{MV}$) have TREE + Y concentrations averaging 0.59 wt.% (Supplementary Table 2). Apatite inclusions in pyrite ($Ap_{PY}$) have high TREE + Y concentrations, averaging 5.56 wt.%, with a maximum of 7.15 wt.%. From the pyrite core to rim, the apatite inclusions show decreasing LREE concentrations and increasing HREE concentrations.

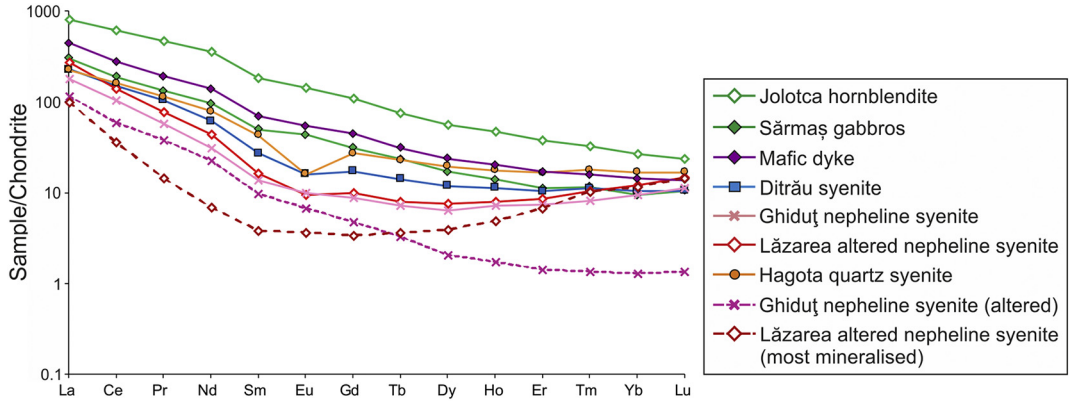


**Fig. 10.** Chondrite normalised REE diagram for representative samples of different lithologies in the Ditrău Complex. Normalising values from McDonough and Sun (1995).

Pyrite grains are commonly fractured and apatite inclusions adjacent to the fractures have altered rims. The rims are depleted in La and Ce. This is at odds with the enrichment seen in apatite alteration rims in carbonate veins in the LANS ($Ap_{CV}$).

The $Ap_{PY}$ hosts two geochemically distinct populations of inclusions. One population is enriched in LREE (monazite) and the other is enriched in HREE (xenotime).

*5.3.5. REE substitution mechanisms into apatite*

Apatites from the mineralised veins ($Ap_{PY}$ and $Ap_{MV}$), have a positive correlation between Na and REE, with low Si, suggesting the substitution mechanism is likely to be: $REE^{3+} + Na^{+} = 2Ca^{2+}$ for these lithologies (Pan and Fleet, 2002; Fig. 12).

A different mechanism controls the substitution of REE into apatites from the LANS ($Ap_{LANS}$, $Ap_{BV}$, $Ap_{CV}$ and $Ap_{APLITIC}$). These have a positive correlation between REE and $SiO_2$, a negative correlation between REE and $P_2O_5$, and no correlation between REE and $Na_2O$. The calculated Si, P and Na cation content suggests the REE enrichment is due to the substitution: $REE^{3+} + SiO_4^{4-} = Ca^{2+} + PO_4^{3-}$ (Fleet and Pan, 1995; Pan and Fleet, 2002; Rønsbo, 1989; Fig. 12). Other charge-compensating mechanisms can achieve the substitution of $Ca^{2+}$ for $REE^{3+}$, potentially the mechanism: $2REE^{3+}$ + vacancy = $3Ca^{2+}$ (Pan and Fleet, 2002), but this is not supported by our data. There is variation within the LANS apatites, apatites closer to the intrusion margin (sample DD23) are aligned with the mineralised veins (Fig. 12). Apatites associated with allanite in the mineralised veins have a higher average Ca concentration, indicating substitution by $REE^{3+} + SiO_4^{4-} = Ca^{2+} + PO_4^{3-}$; however, REE in $Ap_{ALN}$ are low and the high Ca could be due to the association with allanite.

The calculated Na and Si cation content for $Ap_{JH}$ shows that the REE enrichment is a contribution from two substitutions: $REE^{3+} + Na^{+} = 2Ca^{2+}$ and $REE^{3+} + SiO_4^{4-} = Ca^{2+} + PO_4^{3-}$ (Pan and Fleet, 2002; Fig. 12).

## 6. Discussion

The Ditrău Complex mineralisation has formed through the interplay of magmatic and hydrothermal processes, which are discussed below in turn.

### 6.1. Magmatic processes

*6.1.1. Formation of ultramafic cumulates*

Previous work on the Ditrău Complex suggested a number of different genetic models, including metasomatism of the country rock, pulsed intrusions over a long time period, and differentiation in a magma chamber. We propose a model of a magma chamber (Fig. 13) that has been tilted subsequent to emplacement. The petrologic and whole-rock geochemical data presented here are consistent with evolution by fractional crystallisation of an alkaline parental magma. However, it should be noted that recent work by Batki et al. (2018) on clinopyroxenes, suggests two major magma sources, with geochemical trends being explained by repeated introduction of magmatic pulses. The ultramafic cumulates (Jolotca hornblendite) are amphibole-dominated and our observations corroborate those of Pál-Molnár et al. (2015a) who concluded that these are cumulates, crystallised from a basanitic parental magma, and built up in a vertical succession; extensive modal titanite and apatite imply a relatively volatile-rich magma (Morogan et al., 2000). The ultramafic cumulates have the highest magmatic lithology whole-rock REE concentration, and are enriched in Ta, Nb and Ti relative to the other magmatic rocks. Cumulate titanite is modally significant in these rocks and the high partition coefficients of HFSE into titanite make it an important host (Tiepolo et al., 2002).

Morogan et al. (2000) attributes a generalised increase in Nb/Ta, from mafic to evolved compositions, to titanite fractionation. During early crystallisation of the Ditrău Complex, the REE behaved compatibly and were incorporated into cumulus minerals such as titanite (Morogan et al., 2000) and apatite. This indicates early REE saturation in the magma, with the REE removed from the melt before the more evolved lithologies crystallised; similarly, early crystallisation of REE-bearing minerals is observed in the Loch Loyal Syenite Complex in the UK (Walters et al., 2013).

**Table 4**
Nomenclature for the analysed apatites. The apatite mineral chemistry is presented using these abbreviations.

| Lithology | Sample number | Apatite Abbreviation |
|---|---|---|
| Jolotca hornblendite | DJ39 | $Ap_{JH}$ |
| Lăzarea altered nepheline syenite (LANS) | DL15 | $Ap_{LANS}$ |
| Lăzarea altered nepheline syenite (LANS) | DD23 | $Ap_{LANS}$ |
| Aplitic syenite vein cutting LANS | DL10 | $Ap_{APLITIC}$ |
| Biotite vein cutting LANS | DL12 | $Ap_{BV}$ |
| Carbonate vein cutting LANS | DL14 | |
| Large apatites | | $Ap_{CV(L)}$ |
| Small apatites | | $Ap_{CV(S)}$ |
| Mineralised vein apatite | | |
| Apatite adjacent to allanite | DJ40 | $Ap_{ALN}$ |
| Apatite hosted in the carbonate gangue | DJ42 | $Ap_{MV}$ |
| Apatite inclusions in large pyrite grains | DJ42 | $Ap_{PY}$ |

*6.1.2. Enrichment in evolved magmas*

Early amphibole and titanite crystallisation results in the more evolved magmas (syenites and nepheline syenites) having low Mg, Ti, Fe and Ca concentrations. Total alkalis are high throughout crystallisation, and an inflection in $Al_2O_3$ and $Na_2O$ concentrations at c. 55 wt.% $SiO_2$ is considered to mark the onset of alkali feldspar fractionation and nepheline accumulation.

The early crystallisation of titanite and apatite means that REE and HFSE concentrations are relatively low in the Ghiduţ nepheline syenite. The REE pattern is weakly concave. For titanite, MREE have higher partition coefficients than LREE or HREE (Green and Pearson, 1987; Tiepolo et al., 2002). Such a pattern could, therefore, form by early titanite crystallisation or zircon accumulation.

The HREE have a high partition coefficient for zircon relative to LREE (Fujimaki et al., 1984; Thomas et al., 2002), therefore accumulation of zircon would lead to an enrichment of the rock in HREE (Sheard et al., 2012). Petrographic evidence supports zircon accumulation within the Ghiduţ nepheline syenite, reflecting the miaskitic and alkaline nature of the Ditrău Complex. Two generations of zircon are recognised: inclusion-rich zircon and compositionally homogenous zircon (often with a rim of inclusion-rich zircon). The homogenous zircon crystallised deeper in the magma chamber, when zircon first reached the liquidus. The inclusion-rich zircon crystallised in-situ in the more evolved lithologies, as the inclusions are continuous with the surrounding matrix.

The accumulation of magmatic zircon contributes towards the relatively high Hf, Zr, U and Th concentrations in the Ghiduţ nepheline syenite, which is also enriched in Nb relative to Ta. Other processes may also have contributed to this; Batki et al. (2018) proposes that a new parental melt, rich in Nb, Hf and Zr, was introduced and fractionated towards nepheline syenite compositions.

Fall et al. (2007) studied fluid inclusions from the Ghiduţ nepheline syenite and identified a co-existing high salinity, carbonate-rich aqueous fluid with 20–40 wt.% NaCl, which was interpreted to have exsolved from the melt during crystallisation, implying an active magmatic hydrothermal system existed during much of the crystallisation. The relatively high Cl content in the Jolotca hornblendite apatites indicates that this magmatic hydrothermal system developed post-ultramafic cumulate formation.

The most extensive magmatic-hydrothermal alteration occurred in the LANS, and therefore only limited information about magmatic processes can be gleaned from this unit. It is interpreted as originally being a roof-zone nepheline syenite, less evolved than the Ghiduţ

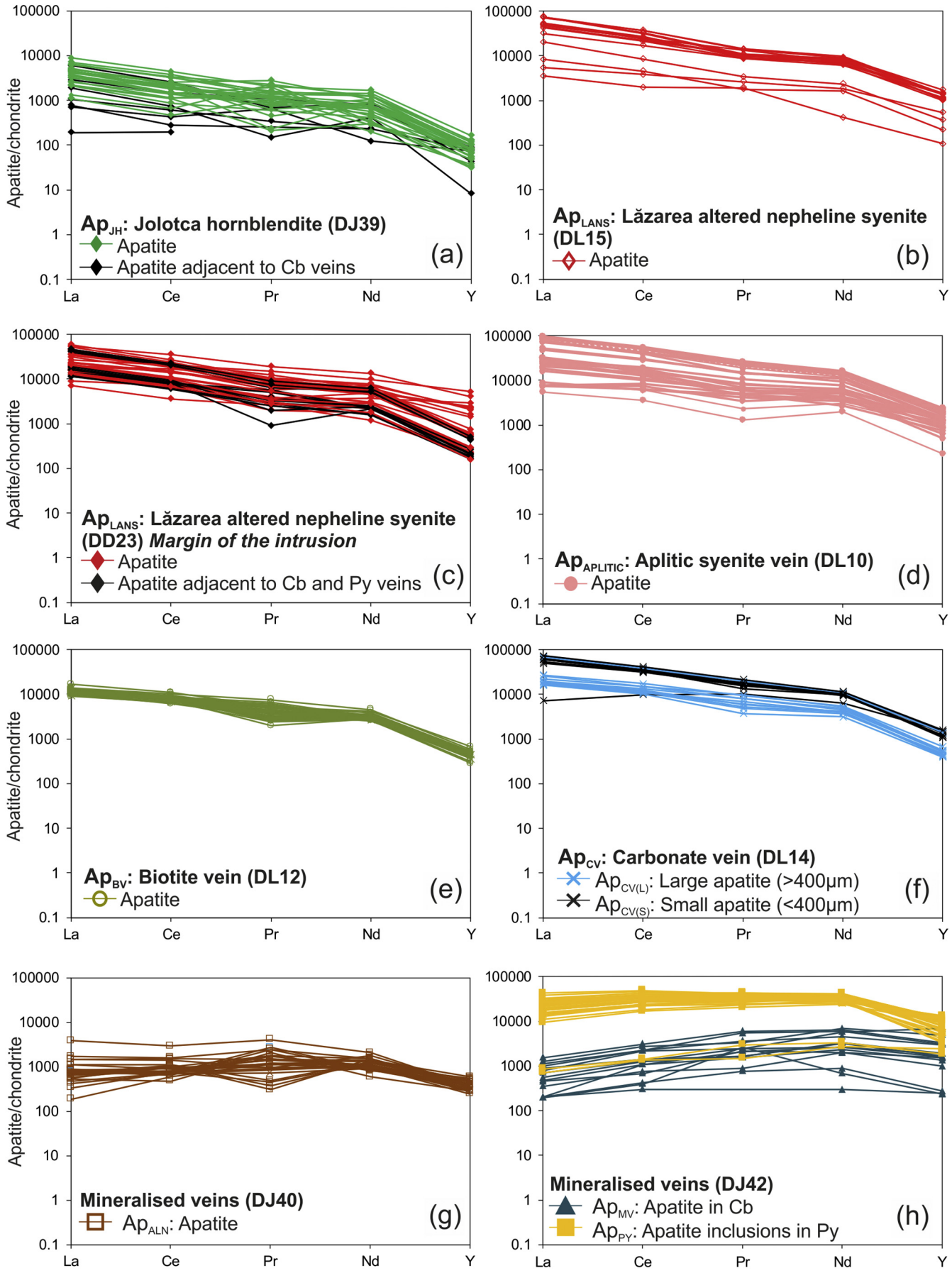
Apatite/chondrite
100000
10000
1000
100
10
1
0.1
La
Ce
Pr
Nd
Y
Ap$_{JH}$: Jolotca hornblendite (DJ39)
Apatite
Apatite adjacent to Cb veins
(a)
Ap$_{LANS}$: Lăzarea altered nepheline syenite (DL15)
Apatite
(b)
Ap$_{LANS}$: Lăzarea altered nepheline syenite (DD23) *Margin of the intrusion*
Apatite
Apatite adjacent to Cb and Py veins
(c)
Ap$_{APLITIC}$: Aplitic syenite vein (DL10)
Apatite
(d)
Ap$_{BV}$: Biotite vein (DL12)
Apatite
(e)
Ap$_{CV}$: Carbonate vein (DL14)
Ap$_{CV(L)}$: Large apatite (>400μm)
Ap$_{CV(S)}$: Small apatite (<400μm)
(f)
Mineralised veins (DJ40)
Ap$_{ALN}$: Apatite
(g)
Mineralised veins (DJ42)
Ap$_{MV}$: Apatite in Cb
Ap$_{PY}$: Apatite inclusions in Py
(h)

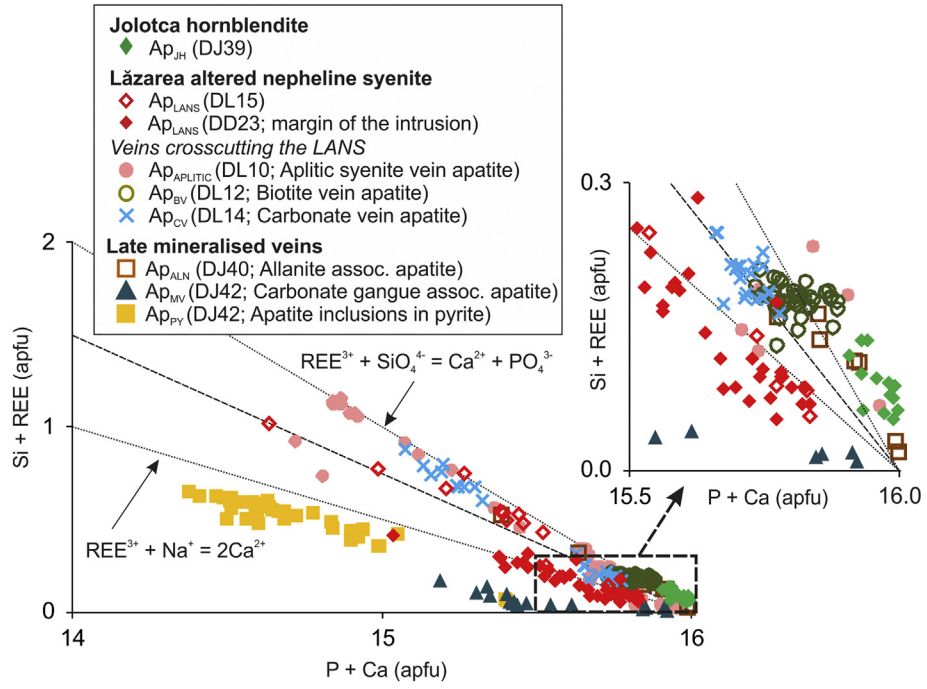


**Fig. 12.** Substitution of REEs into apatite. The dashed line represents an equal contribution from the two substitutions: $REE^{3+} + SiO_4^{4-} = Ca^{2+} + PO_4^{3-}$ and $REE^{3+} + Na^+ = 2Ca^{2+}$, lines plotted as of Pan and Fleet (2002).

nepheline syenite. The fluorapatites within the LANS are considered magmatic from the mineral chemistry and textural relationships.

$Ap_{LANS}$ has the same magmatic REE pattern as $Ap_{JH}$, but with greater REE concentrations; such patterns are common in nepheline syenites e.g. the Pilanesberg Alkaline Complex in South Africa (Liferovich and Mitchell, 2006). Experimental and natural assemblage data have shown that REE uptake in apatite is highest for MREE, forming a convex pattern (Fleet and Pan, 1995; Rønsbo, 2008; Watson and Green, 1981). Given the shape of the Ditrău apatite REE mineral data, it suggests that crystallisation conditions were not constant and the parental melt was LREE-enriched.

Differing REE coupled substitution mechanisms are observed in the analysed apatite especially in the LANS where the mechanism appears related to the position in the intrusion. A key control on REE partitioning into apatite is the melt composition. Generally, melt REE concentrations increase with fractionation (Larsen, 1979). As the degree of polymerization increases, there is a decrease in the number of melt sites suitable for $REE^{3+}$ (Pan and Fleet, 2002). Consequently, $Ap_{LANS}$ has high TREE concentrations (La + Ce up to 5.5 wt.%). The Si-coupled substitution reaction is dominant in magmatic apatite in the Ditrău Complex; as the magma fractionated, melt Si concentration would increase, causing increased polymerization. Fewer melt sites would be suitable for REE and the high Si content would have promoted the coupled substitution: $Ca^{2+} + P^{5+} = REE^{3+} + Si^{4+}$ (Pan and Fleet, 2002). $SiO_2$ will not buffer this coupled substitution as the melt is evolved, therefore the apatite REE record is assumed to reflect that of the melt, for these samples. The LANS marginal sample is from the roof zone immediately adjacent to the country rock and apatite here has a different substitution mechanism to the other LANS apatite. The sample was uniquely associated with fluorite, indicating that magmatic conditions near the margins could have been different and so caused the substitution reaction to change.

The Hagota quartz syenite is silica-saturated and thus diverges from the nepheline syenite fractionation trend and $Na_2O$ Harker plot trend. It is not possible for nepheline syenite and quartz syenite to evolve from the same magma by fractional crystallisation alone (Gill, 2010), and so extrinsic factors are required for magma differentiation to produce a silica-saturated melt. The most likely explanation for this is crustal assimilation (Morogan et al., 2000; Pál-Molnár et al., 2015b). Morogan et al. (2000) measured $\delta^{18}O$ for quartz syenite, with values of 6.1 and 7.7 (‰ V-SMOW). These were higher relative to the rest of the Ditrău Complex, indicating that crustal assimilation played a role in the melt.

### 6.1.3. Magmatic-hydrothermal processes

A magmatic-hydrothermal system is considered to have developed in the latter stages of crystallisation, and is evident in the alteration of the Ghiduţ nepheline syenite, and the highly altered LANS.

*6.1.3.1. Sodic alteration.* The earliest stages of this alteration are apparent in the Ghiduţ nepheline syenite, which has extensive cancrinite development along nepheline grain boundaries. Nepheline breaks down to cancrinite with the addition of (1) calcium carbonate, or (2) a complex carbonate:

(1) $6\ NaAlSiO_4 + 1.5\ CaCO_3 + 1.1\ H_2O = Na_6Ca_{1.5}(AlSiO_4)_6(CO_3)_{1.5}\ 1.1\ H_2O$

has been experimentally determined at 750–1000 °C (Edgar, 1964; Sirbescu and Jenkins, 1999).

(2) $6\ NaAlSiO_4 + 2\ Ca(Cl_2, CO_3, SO_4) + H_2O = Na_6Ca_{1.5}(AlSiO_4)_6(Cl_2, CO_3, SO_4)_2\ 1.1\ H_2O$

forming at 400–500 °C (Fall et al., 2007).

Small veins of calcite cut the Ghiduţ nepheline syenite, indicating the presence of a late-stage carbonate fluid, which promoted alteration of nepheline to cancrinite. Nepheline grains are typically not completely replaced by cancrinite, therefore the reaction was buffered by the volume of fluid or the concentration of carbonate in the fluid.

The Ghiduţ nepheline syenite is also characterised by rarer occurrences of interstitial sodalite along nepheline grain boundaries; this is a high temperature, low pressure phase in which chlorine is an essential component (Sharp et al., 1989). It is common in hydrothermally altered

**Fig. 11.** Chondrite-normalised apatite REE concentrations for La, Ce, Pr, Nd and Y, after McDonough and Sun (1995). (a) Jolotca hornblendite, DJ39. (b) Lăzarea altered nepheline syenite (LANS), DL15. (c) LANS, DD23. (d) Aplitic syenite vein, DL10. (e) Biotite-rich vein, DL12. (f) Carbonate vein, DL14. (g) Mineralised vein, DJ40. (h) Mineralised vein, DJ42.

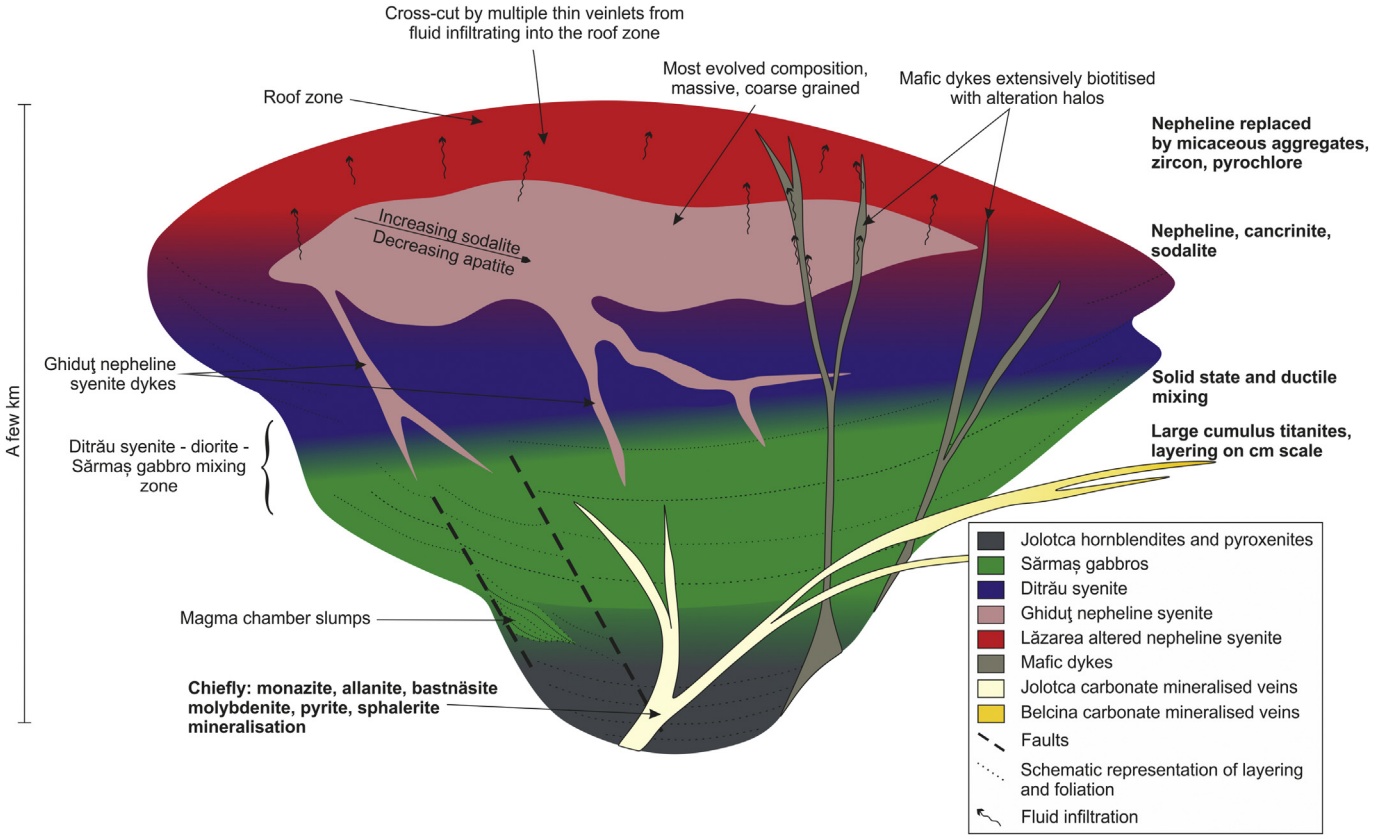


**Fig. 13.** A schematic conceptual model for the Ditrău Complex. The complex is restored to horizontal.

igneous rocks but can be a primary phase in alkali layered intrusions (Eby et al., 1998; Finch, 1991). It forms hydrothermally through the reaction:

$6\ NaAlSiO_4 + 2\ NaCl = Na_8Al_6Si_6O_{24}Cl_2$ (Finch, 1991; Sharp et al., 1989)

Fall et al. (2007) reported a high-salinity fluid present during crystallisation of the Ghiduţ nepheline syenite, with a lower salinity fluid trapped as fluid inclusions in cancrinite. This decrease in salinity indicates the uptake of Na and Cl by cancrinite and sodalite during the early alteration of the nepheline syenites (Fall et al., 2007).

Albitisation also requires Na; although not pervasive, recrystallised albite occurs in patches in the Ghiduţ nepheline syenite, suggesting a Na-rich fluid flushed through (Hövelmann et al., 2010). Breakdown of Na-pyroxene (aegirine) has led to the formation of a well-defined albite reaction rim hosting magnetite and pyrochlore; crystallisation of magnetite and pyrochlore requires the addition of Fe and Nb cations from the fluid. The data indicate that the earliest stages of alteration, evident in the Ghiduţ nepheline syenite, were due to exsolution of a NaCl-rich fluid from the evolving alkaline magma, as proposed by Fall et al. (2007). This fluid may have been relatively rich in Nb, but it did not produce any significant critical metal mineralisation.

*6.1.3.2. Potassic alteration – fluid pathways.* The second type of alteration recognised in the Ghiduţ nepheline syenite is associated with the mafic dykes. These dykes are typically amphibole-rich, and are often altered to biotite, or have significant development of biotite along their margins. Biotitisation of hornblende is known to follow the generalised reaction:

hornblende + $K_2SO_4$ + $H_2SO_4$ = biotite + anhydrite + quartz from experimental work (Brimhall et al., 1985; Speer, 1987).

Alteration of hornblende by a potassic-fluid is considered the main process causing biotitisation of the mafic dykes. We suggest that the margins of the dykes represent pathways for potassic-rich fluids percolating through the Ditrău Complex. The analysed mafic dyke sample is notably more potassic-rich than other mafic lithologies (Fig. 9).

The mafic dyke in the Ditrău valley has a 1–2 m alteration zone in the surrounding Ghiduţ nepheline syenite. This zone is characterised by perthite, alteration of nepheline to micaceous aggregates, and biotite replacing amphibole. This mineral assemblage is characteristic of alteration by potassic fluids. The alteration halo is depleted in REE and HFSE (Zr, Hf, Y, Ta and Nb) relative to the Ghiduţ nepheline syenite (Fig. 9), but not in LFSE. This is unexpected, as HFSE are commonly regarded as immobile in geological systems (Gill, 2010; Pearce and Cann, 1973). However, recent observations and experimental work show that Zr, REE, Y, Nb, Th and U can be mobilised in alkali and F-rich systems (Ayers et al., 2012; Bernini et al., 2013; Mccreath et al., 2012; Sheard et al., 2012; Wilke et al., 2012; Williams-Jones et al., 2012; Yang et al., 2014). Sheard et al. (2012) suggest that LREE were transported as fluoride complexes in magmatic-hydrothermal fluids in the Thor Lake deposit and Williams-Jones et al. (2012) showed that chloride complexes are successful at mobilising REE.

The depletion of Zr and Hf suggests removal of zircon from the Ghiduţ nepheline syenite by fluid using the mafic dyke as a pathway. No zircon has been observed from petrographic study of the mafic dyke alteration halo, despite the abundance of zircon elsewhere in the Ghiduţ nepheline syenite. Geisler et al. (2001) undertook hydrothermal experiments on zircon at 450 °C and 1.3 kbar; these produced zircon reaction rims depleted in Pb, Zr, Si and Th. The experimental conditions are comparable to those inferred for the Ditrău Complex (Fall et al., 2007). If the zircon lattice was damaged by alpha-decay, the zircon would be more susceptible to alteration (Geisler et al., 2001; Silver and Deutsch, 1963; Sinha et al., 1992), this is a possibility for the Ghiduţ nepheline syenite zircons, despite no radiation halos being observed.

Alternatively, the inclusion-rich zones of the zircon may be more vulnerable to breakdown in the presence of a fluid.

Overall, a buoyant potassic-fluid utilised the mafic dykes as channels, enabling upward migration of the fluids through the complex. This fluid was likely rich in ligands such as F and Cl, and so had a leaching effect on the surrounding rocks, sequestering HFSE. The origin of this fluid is not clear, although it should be noted that potassic-rich fluid alteration haloes are a common feature associated with carbonatites (Elliott et al., 2018).

*6.1.3.3. Potassic alteration – deposition in the roof zone.* The LANS is considered to represent the roof zone of the Ditrău Complex and shows pervasive alteration of nepheline to micaceous aggregates, with no cancrinite. The LANS has the highest $K_2O$ and high $Al_2O_3$ whole-rock concentrations, but low CaO and $Na_2O$ concentrations (Fig. 5). Replacement of nepheline by micaceous aggregates is reported in the literature, with the alteration fluid inferred to be potassic-rich, and the alteration of nepheline to micaceous aggregates known to release Na (Rimsaite, 1975). It is plausible that the Na released during nepheline alteration was removed by fluids and is now in the country rocks (fenites).

In the LANS, fracture infills up to 1 mm in width are ubiquitous and these concentrate HFSE-bearing and some REE-bearing minerals, e.g. zircon, pyrochlore, some monazite, bastnäsite, and allanite. The potassic-fluids utilised the cross-cutting mafic dykes as pathways through the complex. They leached REE and HFSE from the surrounding Ghiduţ nepheline syenite as they migrated upwards, then accumulated in the roof zone, altering the nephelines to micaceous aggregates and causing increased fluid pressure on the solidified roof zone (originally a nepheline syenite), resulting in multiple, pervasive micro-fractures. The fluid that accumulated in the roof zone had elevated K, Zr, Nb and Hf concentrations. As the roof zone rock fractured, the decrease in pressure led to crystallisation of the hydrothermal mineral assemblages along the fractures. These phases significantly elevate the whole-rock concentrations of HFSE in the LANS, but the LANS shows little evidence of REE enrichment. It is possible that the REE were preferentially concentrated into a Na-rich fluid that was subsequently expelled from the roof zone.

*6.1.4. Late-stage hydrothermal processes: REE mineralised veins*

Mineralised veins cut the mafic lithologies at Jolotca and the country rock at Belcina (Hirtopanu et al., 2013b); historical mining, field, and mineralogical evidence indicate that these post-date the crystallisation of the magmatic rocks. The absolute age of the mineralised veins is not known. The mineralised veins at both localities are characterised by multiple REE-bearing phases hosted in a carbonate gangue, and appear to be of hydrothermal origin, as suggested by Hirtopanu et al. (2013a, 2013b). The available evidence indicates the veins at Belcina were formed by similar processes to those at Jolotca.

The mineralised veins have previously been explored for REE, and their mineralogy clearly indicates high REE concentrations. The fluid that transported the REE in was carbonate-rich, and to dissolve the REE, it must also have contained ligands such as F or Cl (Williams-Jones et al., 2012). This fluid could have been derived from the magmatic system, possibly by late-stage immiscibility within the magma chamber, as REE preferentially partition into a carbonate-rich fluid rather than a silicate fluid (Mitchell, 2005); or it could have been derived from a separate source, possibly associated with late carbonatitic magmas. A clue to resolving this comes from the apatite chemistry; apatite holds a host of REE information (Chakhmouradian et al., 2017).

Small carbonate veins are present within the Ghiduţ nepheline syenite and LANS, and likely formed by late-stage exsolution of a carbonate-rich fluid in the magmatic-hydrothermal system. The carbonate vein apatites in the LANS ($Ap_{CV}$) have elevated concentrations of LREE, with a linear decreasing pattern, whereas the apatites from mineralised veins with a carbonate gangue have convex patterns with much higher concentrations of Y. Noticeably, $Ap_{CV}$ do not have the same substitution mechanism as the apatite in the carbonate gangue of the mineralised veins. This strongly indicates that the mineralised veins in the Jolotca area are derived from different fluids to those involved in alteration of the LANS.

Hirtopanu et al. (2013a) suggest the magmatic events concluded with a carbonatite melt, which followed the pathways of previous melts, and was the source for the mineralising vein fluids. Late-stage carbonatites are certainly common in similar alkaline igneous complexes (e.g. Harmer, 1999; Verhulst et al., 2000), and there are at least two different phases of carbonate-rich fluid. Furthermore, the potassic-rich fluid that caused alteration of the mafic dykes and the LANS could originate from the carbonatite magmatism, as is typical in fenites (Elliott et al., 2018). It is thus clear that emplacement of a later carbonatite at depth, with release of potassic-rich and carbonate-rich mineralising fluids into the complex, is a plausible explanation for the mineralisation at Ditrău. Further work would be needed to prove this hypothesis.

## 7. Conclusions

The Ditrău Complex is an alkaline intrusion which was subsequently tilted during the Variscan orogeny. Fractional crystallisation in the magma chamber produced highly evolved nepheline syenites, but REE behaved compatibly at an early stage within the crystallising melt and were preferentially incorporated into titanite and apatite in ultramafic cumulates.

A hydrothermal system developed within the Ditrău Complex magma chamber during crystallisation, with patchy alteration of the nepheline syenites by a sodic fluid, and replacement of nepheline by cancrinite and sodalite. Subsequently, mafic dykes provided conduits for the upward migration of late stage potassic-fluids, which leached REE and HFSE from the Ghiduţ nepheline syenite. These fluids reached the roof zone of the complex where they were trapped and percolated through, causing the breakdown of nepheline to K-rich pseudomorphs and the deposition of hydrothermal minerals, such as zircon and pyrochlore. The roof zone does not show significant REE mineralisation.

The REE mineralisation is hosted in carbonate-rich veins that cross-cut the complex and are known from the Jolotca and Belcina regions. From apatite mineral chemistry and petrologic study, they are compositionally distinct from the other lithologies, including the altered roof zone. We consider the mineralised veins at Jolotca and Belcina to be related to the same late REE- and carbonate-rich fluid, with pH controlled REE deposition. The fluid source could be a late-stage carbonatite emplaced below the complex, as seen in the Spitskop Complex or Kovdor intrusion, for example (Harmer, 1999; Verhulst et al., 2000) but further work is required to prove a carbonatitic source.

Supplementary data to this article can be found online at https://doi.org/10.1016/j.lithos.2018.05.029.

## Acknowledgements

Many thanks to Strategic Resources Ltd. for fieldwork assistance and Gyula Jakab for fieldwork advice. Thanks to Michael Stock and Victoria Smith at the University of Oxford and Chris Hayward from the University of Edinburgh for apatite EPMA advice, and Alicja Lacinska, Gren Turner and Jeremy Rushton at the British Geological Survey, Keyworth, for SEM help and advice. VCH acknowledges support from the Warwickshire Geological Conservation Group through their Holloway Award and the British Geological Survey for BUFI funding for an MSc project. VCH is supported by a Natural Environment Research Council studentship, grant number LBAG/175. KMG and RAS publish with the permission of the Executive Director of the British Geological Survey. This work is a contribution to the EURARE project, which was funded by the European Community's Seventh Framework Programme under grant agreement no. 309373. This work benefited from detailed and useful reviews from E. Pál-Molnár and J. Kynicky.

## References


Anastasiu, N., Constantinescu, E., 1982. Tectonostructural position of the foidic rocks in the Romanian Carpathians. Ser. Geol. Bucuresti. 26, 33–45.

Ayers, J., Zhang, L., Luo, Y., Peters, T., 2012. Zircon solubility in alkaline aqueous fluids at upper crustal conditions. Geochim. Cosmochim. Acta 96, 18–28.

Batki, A., Pál-Molnár, E., Dobosi, G., Skelton, A., 2014. Petrogenetic significance of ocellar camptonite dykes in the Ditrău Alkaline Massif, Romania. Lithos 200–201, 181–196.

Batki, A., Pál-Molnár, E., Jankovics, M.É., Kerr, A.C., Kiss, B., Markl, G., Heincz, A., Harangi, S., 2018. Insights into the evolution of an alkaline magmatic system: an in situ trace element study of clinopyroxenes from the Ditrău alkaline massif, Romania. Lithos 300, 51–71.

Bernini, D., Audétat, A., Dolejš, D., Keppler, H., 2013. Zircon solubility in aqueous fluids at high temperatures and pressures. Geochim. Cosmochim. Acta 119, 178–187.

Binnemans, K., Jones, P.T., Blanpain, B., Van Gerven, T., Yang, Y., Walton, A., Buchert, M., 2013. Recycling of rare earths: a critical review. J. Clean. Prod. 51, 1–22.

Brimhall, G.H., Agee, C., Stoffregen, R., 1985. The hydrothermal conversion of hornblende to biotite. Can. Mineral. 23, 369–379.

Chakhmouradian, A.R., Wall, F., 2012. Rare earth elements: minerals, mines, magnets (and more). Elements 8, 333–340.

Chakhmouradian, A.R., Reguir, E.P., Zaitsev, A.N., Couëslan, C., Xu, C., Kynický, J., Mumin, A. H., Yang, P., 2017. Apatite in carbonatitic rocks: compositional variation, zoning, element partitioning and petrogenetic significance. Lithos 274-275, 188–213.

Codarcea, A., Codarcea-Dessila, M., Ianovici, V., 1957. Structure géologique du massif des roches alcalines de Ditrau. Rev. Géol. Géogr. Acad. Rom. II, 3–4.

Commision, E., 2017. Study on the review of the list of critical raw materials, industrial policy. Trade — Competition. EU:1–93 https://doi.org/10.2873/876644 978-92-79-47937-3.

Constantinescu, E., Anastasiu, N., 1979. Nepheline from the alkaline massif of Ditrău. Analele Univ. Buc. Geol. 18, 15–27.

Dallmeyer, R., Catalán, J.M., Arenas, R., Ibarguchi, J.G., Gutiérrez, G., Farias, P., Bastida, F., Aller, J., 1997. Diachronous Variscan tectonothermal activity in the NW Iberian Massif: evidence from 40Ar/39Ar dating of regional fabrics. Tectonophysics 277, 307–337.

Dewey, J.F., Pitman, W.C., Ryan, W.B., Bonnin, J., 1973. Plate tectonics and the evolution of the Alpine system. Geol. Soc. Am. Bull. 84, 3137–3180.

Eby, G.N., Woolley, A.R., Din, V., Platt, G., 1998. Geochemistry and petrogenesis of nepheline syenites: Kasungu–Chipala, Ilomba, and Ulindi nepheline syenite intrusions, North Nyasa Alkaline Province, Malawi. J. Petrol. 39, 1405–1424.

Edgar, A., 1964. Studies on cancrinites; part 2, stability fields and cell dimensions of calcium and potassium-rich cancrinites. Can. Mineral. 8, 53–67.

Elliott, H.A.L., Wall, F., Chakhmouradian, A.R., Siegfried, P.R., Dahlgren, S., Weatherley, S., Finch, A.A., Marks, M.A.W., Dowman, E., Deady, E., 2018. Fenites associated with carbonatite complexes: a review. Ore Geol. Rev. 93, 38–59.

Fall, A., Bodnar, R.J., Szabó, C., Pál-Molnár, E., 2007. Fluid evolution in the nepheline syenites of the Ditrău Alkaline Massif, Transylvania, Romania. Lithos 95, 331–345.

Finch, A.A., 1991. Conversion of nepheline to sodalite during subsolidus processes in alkaline rocks. Mineral. Mag. 55 459-316H.

Fleet, M.E., Pan, Y., 1995. Site preference of rare earth elements in fluorapatite. Am. Mineral. 80, 329–335.

Fujimaki, H., Tatsumoto, M., Aoki, K.i., 1984. Partition coefficients of Hf, Zr, and REE between phenocrysts and groundmasses. J. Geophys. Res. Solid Earth 89.

Geisler, T., Ulonska, M., Schleicher, H., Pidgeon, R.T., van Bronswijk, W., 2001. Leaching and differential recrystallization of metamict zircon under experimental hydrothermal conditions. Contrib. Mineral. Petrol. 141, 53–65.

Gill, R., 2010. Igneous Rocks and Processes: A Practical Guide. John Wiley & Sons.

Gillespie, M., Styles, M., 1999. BGS Rock Classification Scheme. Classification of Igneous Rocks. vol. 1.

Goodenough, K., Schilling, J., Jonsson, E., Kalvig, P., Charles, N., Tuduri, J., Deady, E., Sadeghi, M., Schiellerup, H., Müller, A., 2016. Europe's rare earth element resource potential: an overview of REE metallogenetic provinces and their geodynamic setting. Ore Geol. Rev. 72, 838–856.

Green, T., Pearson, N., 1987. An experimental study of Nb and Ta partitioning between Ti-rich minerals and silicate liquids at high pressure and temperature. Geochim. Cosmochim. Acta 51, 55–62.

Harmer, R.E., 1999. The Petrogenetic Association of Carbonatite and Alkaline Magmatism: constraints from the Spitskop Complex, South Africa. J. Petrol. 40, 525–548.

Hirtopanu, P., Andersen, J., Fairhurst, R., 2010. Nb, Ta, REE (Y), Ti, Zr, Th, U and Te rare element minerals within the Ditrău alkaline intrusive complex, eastern Carpathians, Romania. Mineralogy of Székelyland, Eastern Transylvania, Romania. Csik County Nature and Conservation Society, Miercurea Ciuc, pp. 89–128.

Hirtopanu, P., Andersen, J.C., Fairhurst, R.J., Jakab, G., 2013a. Allanite-(Ce) and its associations, from the Ditrau alkaline intrusive massif, East Carpathians, Romania. Proceed. Roman. Acad. Ser. B 15, 59–74.

Hirtopanu, P., Jakab, G., Andersen, C., Fairhurst, J., 2013b. Thorite, thorogummite and xenotime-(Y) occurrence in Ditrau alkaline intrusive massif, East Carpathians, Romania. Proceed. Roman. Acad. Ser. B 15, 111–132.

Hirtopanu, P., Fairhurst, R.J., Jakab, G., Andersen, C., 2015. Niobian rutile and its associations at Jolotca, Ditrau alkaline intrusive massif, east Carpathians, Romania. Proceed. Roman. Acad. Ser. B 17, 39–55.

Hövelmann, J., Putnis, A., Geisler, T., Schmidt, B.C., Golla-Schindler, U., 2010. The replacement of plagioclase feldspars by albite: observations from hydrothermal experiments. Contrib. Mineral. Petrol. 159, 43–59.

Jakab, G., 1998. Geologia Masivului alcalin de la Ditrău. Pallas-Akademia, Miercurea-Ciuc.

Kräutner, H., Bindea, G., 1998. Timing of the Ditrău alkaline intrusive complex (Eastern Carpathians, Romania). Slovak Geological Magazine 4, 213–221.

Larsen, L.M., 1979. Distribution of REE and other trace elements between phenocrysts and peralkaline undersaturated magmas, exemplified by rocks from the Gardar igneous province, south Greenland. Lithos 12, 303–315.

Liferovich, R., Mitchell, R., 2006. Apatite-group Minerals From Nepheline Syenite, Pilansberg Alkaline Complex. De Gruyter, South Africa.

Matenco, L., Krezsek, C., Merten, S., Schmid, S., Cloetingh, S., Andriessen, P., 2010. Characteristics of collisional orogens with low topographic build-up: an example from the Carpathians. Terra Nova 22, 155–165.

Mccreath, J., Finch, A., Simonsen, S., Donaldson, C., Armour-Brown, A., 2012. Independent ages of magmatic and hydrothermal activity in alkaline igneous rocks: the Motzfeldt Centre, Gardar Province, South Greenland. Contrib. Mineral. Petrol. 163, 967–982.

McDonough, W.F., Sun, S.-S., 1995. The composition of the Earth. Chem. Geol. 120, 223–253.

Mitchell, R.H., 2005. Carbonatites and carbonatites and carbonatites. Can. Mineral. 43, 2049–2068.

Miyashiro, A., 1974. Volcanic rock series in island arcs and active continental margins. Am. J. Sci. 274, 321–355.

Morogan, V., Upton, B., Fitton, J., 2000. The petrology of the Ditrau alkaline complex, eastern Carpathians. Mineral. Petrol. 69, 227–265.

Pál-Molnár, E., 2000. Hornblendites and diorites of the Ditró Syenite Massif. Department of Mineralogy, Geochemistry and Petrology, University of Szeged, Szeged, 172 pp..

Pál-Molnár, E., Avra-Sós, E., 1995. K/Ar radiometric dating on rocks from the northern part of the Ditró syenite massif and its petrogenetic implications. Acta Mineral. Petrogr. Szeged. 34, 101–116.

Pál-Molnár, E., Batki, A., Almási, E., Kiss, B., Upton, B.G., Markl, G., Odling, N., Harangi, S., 2015a. Origin of mafic and ultramafic cumulates from the Ditrău Alkaline Massif, Romania. Lithos 239, 1–18.

Pál-Molnár, E., Batki, A., Ódri, Á., Kiss, B., Almasi, E., 2015b. Geochemical implications for the magma origin of granitic rocks from the Ditrău Alkaline Massif (Eastern Carpathians, Romania). Geol. Croatica 68, 51–66.

Pan, Y., Fleet, M.E., 2002. Compositions of the apatite-group minerals: substitution mechanisms and controlling factors. Rev. Mineral. Geochem. 48, 13–49.

Pană, D., Balintoni, I., Heaman, L., 2000. Precise U-Pb zircon dating of the syenite phase from the Ditrau alkaline igneous complex. Stud. UBB Geol. 45, 79–90.

Pearce, J.A., Cann, J., 1973. Tectonic setting of basic volcanic rocks determined using trace element analyses. Earth Planet. Sci. Lett. 19, 290–300.

Piccoli, P.M., Candela, P.A., 2002. Apatite in igneous systems. Rev. Mineral. Geochem. 48, 255–292.

Pyle, J.M., Spear, F.S., Wark, D.A., 2002. Electron microprobe analysis of REE in apatite, monazite and xenotime: protocols and pitfalls. Rev. Mineral. Geochem. 48, 337–362.

Rimsaite, J., 1975. Natural alteration of mica and reactions between released ions in mineral deposits. Clay Clay Miner. 23, 247–255.

Rønsbo, J., 1989. Coupled substitutions involving REEs and Na and Si in apatites in alkaline rocks from the Ilimaussaq intrusion, South Greenland, and the petrological implications. Am. Mineral. 74, 896–901.

Rønsbo, J.G., 2008. Apatite in the Ilímaussaq alkaline complex: occurrence, zonation and compositional variation. Lithos 106, 71–82.

Săbău, G., 2009. Ti-Nb-REE assemblages in the monazite veins at Jolotca, Ditrău alkaline Massif. In: Anastasiu, N., Duliu, O. (Eds.), Mineralogy and Geodiversity - Tributes to the Career of Professor Emil Constantinescu. Universităţii din Bucuresti, pp. 143–153.

Sharp, Z., Helffrich, G., Bohlen, S.R., Essene, E.J., 1989. The stability of sodalite in the system $NaAlSiO_4$-NaCl. Geochim. Cosmochim. Acta 53, 1943–1954.

Sheard, E.R., Williams-Jones, A.E., Heiligmann, M., Pederson, C., Trueman, D.L., 2012. Controls on the concentration of zirconium, niobium, and the rare earth elements in the Thor Lake rare metal deposit, Northwest Territories, Canada. Econ. Geol. 107, 81–104.

Silver, L.T., Deutsch, S., 1963. Uranium-lead isotopic variations in zircons: a case study. J. Geol. 71, 721–758.

Sinha, A.K., Wayne, D.M., Hewitt, D.A., 1992. The hydrothermal stability of zircon: preliminary experimental and isotopic studies. Geochim. Cosmochim. Acta 56, 3551–3560.

Sirbescu, M., Jenkins, D.M., 1999. Experiments on the stability of cancrinite in the system $Na_2O$-CaO-$Al_2O_3$-$SiO_2$-$CO_2$-$H_2O$. Am. Mineral. 84, 1850–1860.

Speer, J.A., 1987. Evolution of magmatic AFM mineral assemblages in granitoid rocks: the hornblende + melt = biotite reaction in the Liberty Hill pluton, South Carolina. Am. Mineral. 72 (United States).

Stampfli, G.M., 2000. Tethyan Oceans. 173. Geological Society, London, pp. 1–23 special publications.

Stock, M.J., Humphreys, M.C., Smith, V.C., Johnson, R.D., Pyle, D.M., EIMF, 2015. New constraints on electron-beam induced halogen migration in apatite. Am. Mineral. 100, 281–293.

Stormer, J., Pierson, M.L., Tacker, R.C., 1993. Variation of F and cl X-ray intensity due to anisotropic diffusion in apatite. Am. Mineral. 78, 641–648.

Streckeisen, A., 1960. On the Structure and Origin of the Nepheline-Syenite Complex of Ditroff (Transsylvania, Rumania). Rep 21th IGC Part 13. pp. 228–238.

Streckeisen, A., Hunziker, J., 1974. On the origin and age of the Nepheline Syenite Massif of Ditro (Transsylvania, Rumania). Schweiz. Mineral. Petrogr. Mitt. 54, 59–77.

Survey, USG, 2015. Mineral commodity summaries 2015. In: Survey, U.S.G. (Ed.), Rare Earths.

Szakacs, A., Ioane, D., Seghedi, I., Rogobete, M., Pecskay, Z., 1997. Rates of migration of volcanic activity and magma out put along the Calimani-Gurghiu-Harghita volcanic range, East Carpathians, Romania. Prz. Geol. 45, 1106.

Thomas, J., Bodnar, R., Shimizu, N., Sinha, A., 2002. Determination of zircon/melt trace element partition coefficients from SIMS analysis of melt inclusions in zircon. Geochim. Cosmochim. Acta 66, 2887–2901.

Tiepolo, M., Oberti, R., Vannucci, R., 2002. Trace-element incorporation in titanite: constraints from experimentally determined solid/liquid partition coefficients. Chem. Geol. 191, 105–119.

Vantongeren, J., Mathez, E., 2012. Large-scale liquid immiscibility at the top of the Bushveld Complex, South Africa. Geology 40, 491–494.
Verhulst, A., Balaganskaya, E., Kirnarsky, Y., Demaiffe, D., 2000. Petrological and geochemical (trace elements and Sr–Nd isotopes) characteristics of the Paleozoic Kovdor ultramafic, alkaline and carbonatite intrusion (Kola Peninsula, NW Russia). Lithos 51, 1–25.
Walters, A.S., Goodenough, K.M., Hughes, H.S., Roberts, N.M., Gunn, A., Rushton, J., Lacinska, A., 2013. Enrichment of rare earth elements during magmatic and post-magmatic processes: a case study from the Loch Loyal Syenite Complex, northern Scotland. Contrib. Mineral. Petrol. 166, 1177–1202.
Watson, E.B., Green, T.H., 1981. Apatite/liquid partition coefficients for the rare earth elements and strontium. Earth Planet. Sci. Lett. 56, 405–421.
Whitney, D.L., Evans, B.W., 2010. Abbreviations for names of rock-forming minerals. Am. Mineral. 95, 185–187.
Wilke, M., Schmidt, C., Dubrail, J., Appel, K., Borchert, M., Kvashnina, K., Manning, C.E., 2012. Zircon solubility and zirconium complexation in $H_2O + Na_2O + SiO_2 \pm Al_2O_3$ fluids at high pressure and temperature. Earth Planet. Sci. Lett. 349–350, 15–25.
Williams-Jones, A.E., Migdisov, A.A., Samson, I.M., 2012. Hydrothermal mobilisation of the rare earth elements – a tale of "ceria" and "yttria". Elements 8, 355–360.
Yang, W.-B., Niu, H.-C., Shan, Q., Sun, W.-D., Zhang, H., Li, N.-B., Jiang, Y.-H., Yu, X.-Y., 2014. Geochemistry of magmatic and hydrothermal zircon from the highly evolved Baerzhe alkaline granite: implications for Zr–REE–Nb mineralization. Mineral. Deposita 49, 451–470.
Zincenco, D., Vlad, C., 1978. Studiul geochimic-metalogenetic al masivului Ditrău şi al formaţiunilor adiacente cu privire specială asupra mineralizaţiilor associate, Partea I. Structura, petrografia şi petrologia masivului.